SIAM J. SCI. COMPUT.
Vol. 23, No. 3, pp. 707–740

SEMIDISCRETE CENTRAL-UPWIND SCHEMES FOR HYPERBOLIC CONSERVATION LAWS AND HAMILTON–JACOBI EQUATIONS*

ALEXANDER KURGANOV†, SEBASTIAN NOELLE‡, AND GUERGANA PETROVA†

Abstract. We introduce new Godunov-type semidiscrete central schemes for hyperbolic systems of conservation laws and Hamilton–Jacobi equations. The schemes are based on the use of more precise information about the local speeds of propagation and can be viewed as a generalization of the schemes from [A. Kurganov and E. Tadmor, *J. Comput. Phys.*, 160 (2000), pp. 241–282; A. Kurganov and D. Levy, *SIAM J. Sci. Comput.*, 22 (2000), pp. 1461–1488; A. Kurganov and G. Petrova, *A third-order semidiscrete genuinely multidimensional central scheme for hyperbolic conservation laws and related problems*, Numer. Math., to appear] and [A. Kurganov and E. Tadmor, *J. Comput. Phys.*, 160 (2000), pp. 720–742].

The main advantages of the proposed central schemes are the high resolution, due to the smaller amount of the numerical dissipation, and the simplicity. There are no Riemann solvers and characteristic decomposition involved, and this makes them a universal tool for a wide variety of applications.

At the same time, the developed schemes have an upwind nature, since they respect the directions of wave propagation by measuring the *one-sided* local speeds. This is why we call them *central-upwind* schemes.

The constructed schemes are applied to various problems, such as the Euler equations of gas dynamics, the Hamilton–Jacobi equations with convex and nonconvex Hamiltonians, and the incompressible Euler and Navier–Stokes equations. The incompressibility condition in the latter equations allows us to treat them both in their conservative and transport form. We apply to these problems the central-upwind schemes, developed separately for each of them, and compute the corresponding numerical solutions.

Key words. multidimensional conservation laws and Hamilton–Jacobi equations, high-resolution semidiscrete central schemes, compressible and incompressible Euler equations

AMS subject classifications. Primary, 65M06; Secondary, 35L65

PII. S1064827500373413

1. Introduction.

We consider Godunov-type schemes for the multidimensional (multi-D) systems of conservation laws

$$u_t + \nabla_{\mathbf{x}} \cdot f(u) = 0, \quad \mathbf{x} \in \mathbb{R}^d, \tag{1.1}$$

and the multi-D Hamilton–Jacobi equations

$$\varphi_t + H(\nabla_{\mathbf{x}}\varphi) = 0, \quad \mathbf{x} \in \mathbb{R}^d. \tag{1.2}$$

Godunov-type schemes for the system (1.1) are projection-evolution methods. Starting with cell averages at time level t^n, one reconstructs a piecewise polynomial interpolant of degree $r-1$ (where r is the formal order of the scheme), which is

*Received by the editors June 7, 2000; accepted for publication (in revised form) February 19, 2001; published electronically August 15, 2001.

http://www.siam.org/journals/sisc/23-3/37341.html

†Department of Mathematics, University of Michigan, Ann Arbor, MI 48109-1109 (kurganov@math.lsa.umich.edu, petrova@math.lsa.umich.edu). The first author was supported in part by a NSF Group Infrastructure grant and NSF grant DMS-0073631. The third author was supported by the Rackham Grant and Fellowship Program, and her visit to Bonn University was sponsored by DFG grant SFB256.

‡Institut für Geometrie und Praktische Mathematik, RWTH Aachen, Templergraben 55, 52056 Aachen, Germany (noelle@igpm.rwth-aachen.de). Part of the work of the second author was sponsored by DFG grant SFB256.

evolved to the next time level t^{n+1}, and then it is projected onto a space of piecewise constants. Depending on the projection step, we distinguish two kinds of Godunov-type schemes: central and upwind. The Godunov-type central schemes are based on exact evolution and averaging over Riemann fans. In contrast to the upwind schemes, they do not employ Riemann solvers and characteristic decomposition, which makes them *simple, efficient,* and *universal*.

In the one-dimensional (1-D) case, examples of such schemes are the first-order (staggered) Lax–Friedrichs scheme [28, 14], the second-order Nessyahu–Tadmor scheme [40], and the higher-order schemes in [39, 8, 30]. Second-order multi-D central schemes were introduced in [3, 4, 5, 6, 19, 34], and their higher-order extensions were developed in [31, 32]. We would also like to mention the central schemes for incompressible flows in [33, 22, 20, 21], and their applications to various systems, for example, [2, 13, 44, 49].

Unfortunately, these staggered central schemes may not provide a satisfactory resolution when small time steps are enforced by stability restrictions, which may occur, for example, in the application of these schemes to convection-diffusion problems. Also, they cannot be used for steady-state computations. These disadvantages are caused by the accumulation of numerical dissipation, which is of order $\mathcal{O}(\frac{(\Delta x)^{2r}}{\Delta t})$, where r is the formal order of the scheme.

The aforementioned problems have been recently resolved in [26], where new high-order Godunov-type central schemes are introduced. The proposed construction is based on the use of the CFL related *local speeds of propagation* and on integration over Riemann fans of variable sizes. In this way, a *nonstaggered* fully discrete central scheme is derived and is naturally reduced to a particularly simple semidiscrete form (for details see [26]). The same idea was used in [24] to develop a third-order semidiscrete central scheme, and in [25], where its genuinely multi-D extension was introduced.

The purpose of the first part of this paper is to present new semidiscrete central schemes for the conservation law (1.1), which we call *central-upwind* schemes. They are based on the *one-sided local speeds of propagation*. For example, in the 1-D case, these one-sided local speeds are the largest and smallest eigenvalues of the Jacobian $\frac{\partial f}{\partial u}$ (in contrast to the less precise local information, used in [26, 24, 25]—the spectral radius $\rho(\frac{\partial f}{\partial u})$).

The new schemes are Godunov-type *central* schemes, because the evolution step employs integration over Riemann fans and does not require a Riemann solver and a characteristic decomposition. They also have an *upwind* nature, since one-sided information is used to estimate the width of the Riemann fans. This more precise estimate makes our schemes less dissipative generalizations of the semidiscrete central schemes in [26, 24, 25].

The second part of this paper is devoted to the Hamilton–Jacobi equations, (1.2), which are closely related to (scalar) conservation laws. For example, in the 1-D case, the unique viscosity solution of the Hamilton–Jacobi equation, $\varphi_t + H(\varphi_x) = 0$, is the primitive of the unique entropy solution of the corresponding conservation law, $u_t + H(u)_x = 0$, where $u = \varphi_x$. However, in the multi-D case, this one-to-one correspondence no longer exists, but the gradient $\nabla_{\mathbf{x}}\varphi$ satisfies (at least formally) a system of (weakly) hyperbolic conservation laws.

This relation allows one to apply techniques, developed for conservation laws, to the derivation of the numerical methods for Hamilton–Jacobi equations. Examples of such methods can be found in [1, 10, 11, 35, 36, 42, 48]. One of the approaches [35, 36] is Godunov-type schemes. As in the case of conservation laws, they are projection-

evolution methods. The differences are that here one starts with point values (not cell averages) at time t^n, builds a *continuous* piecewise polynomial reconstruction of degree r, and evolves it to the next time level t^{n+1}. The pointwise projection (not the cell averages) of this evolved solution is used as initial data for the next time step.

Godunov-type central schemes for Hamilton–Jacobi equations were first introduced in [35, 36]. Semidiscrete Godunov-type central schemes for the multi-D equations (1.2) were developed in [27], where the same idea of *local speeds of propagation* was used to separate between smooth and nonsmooth parts of the evolved solution.

In the second part of this work, we present a new second-order semidiscrete central-upwind scheme for the Hamilton–Jacobi equations (1.2). It is a less dissipative generalization of the scheme in [27], which uses more precise one-sided information of the local propagation speeds.

The paper is organized as follows. In section 2, we give a brief overview of the Godunov-type central schemes for conservation laws and Hamilton–Jacobi equations in one space dimension. We also describe the nonoscillatory piecewise quadratic reconstruction from [25], which is later used in the numerical examples. Next, in section 3, we introduce our new Godunov-type *central-upwind* schemes for the conservation laws and Hamilton–Jacobi equations, both in one and in two spatial dimensions. The results of our numerical experiments are presented in section 4. We apply the proposed scheme to a variety of test problems: the one- and two-dimensional compressible Euler equations, a 1-D Hamilton–Jacobi equation with a nonconvex Hamiltonian, the two-dimensional (2-D) eikonal equation of geometric optics. Finally, the incompressible Euler and Navier–Stokes equations are solved using two different approaches, based on either their conservative or transport form. The performed numerical experiments, especially in the case of incompressible flow simulations (see section 4.3), demonstrate the advantage of our new central-upwind approach.

2. Godunov-type central schemes—brief description. In this section, we review Godunov-type central schemes in one spatial dimension. We will consider only uniform grids and use the following notation: let $x_j := j\Delta x$, $x_{j\pm\frac12} := (j \pm 1/2)\Delta x$, $t^n := n\Delta t$, $u_j^n := u(x_j, t^n)$, $\varphi_j^n := \varphi(x_j, t^n)$, where Δx and Δt are small spatial and time scales, respectively.

2.1. Central schemes for conservation laws. The starting point for the construction of Godunov-type schemes for conservation laws is the equivalent integral formulation of the system (1.1),

$$\begin{aligned}&\bar u(x,t+\Delta t)\\ &= \bar u(x,t) - \frac{1}{\Delta x}\left[\int_{\tau=t}^{t+\Delta t} f\left(u\left(x+\frac{\Delta x}{2},\tau\right)\right)d\tau - \int_{\tau=t}^{t+\Delta t} f\left(u\left(x-\frac{\Delta x}{2},\tau\right)\right)d\tau\right],\end{aligned} \tag{2.1}$$

where by

$$\bar u(x,t) := \frac{1}{\Delta x}\int_{I(x)} u(\xi,t)\,d\xi, \qquad I(x) = \left\{\xi : |\xi - x| < \frac{\Delta x}{2}\right\} \tag{2.2}$$

we denote the sliding averages of $u(\cdot,t)$ over the interval $(x-\frac{\Delta x}{2}, x+\frac{\Delta x}{2})$. At time level $t = t^n$ we consider problem (2.1) with the piecewise polynomial initial condition

$$\widetilde u(x,t^n) = p_j^n(x), \qquad x_{j-\frac12} < x < x_{j+\frac12} \quad \forall j, \tag{2.3}$$

obtained from the cell averages $\bar{u}_j^n := \bar{u}(x_j, t^n)$, computed at the previous time step. This piecewise polynomial reconstruction should be conservative, accurate of order r, and nonoscillatory.

Second-order schemes require a piecewise linear reconstruction (see the examples in [15, 16, 23, 29, 40, 43]). Third-order schemes employ a piecewise quadratic approximation, and one of the possibilities is to use the essentially nonoscillatory (ENO) reconstruction. In the 1-D case, we refer the reader to [16, 46]. The weighted ENO interpolants are proposed in [38, 18, 30, 32], and the multi-D ENO-type reconstructions can be found in [31, 32]. The ENO-type approach employs smoothness indicators. They require certain a priori information about the solution, which may be unavailable and then spurious oscillations or extra smearing of discontinuities may appear.

1-D nonoscillatory piecewise quadratic reconstructions, which do not require the use of smoothness indicators, were proposed in [37, 39, 25]. 2-D generalizations of these reconstructions were presented in [25, 41].

The reconstructed piecewise polynomial $\widetilde{u}(x, t^n)$ is then evolved exactly according to (2.1), and the solution at time $t = t^{n+1}$ is obtained in terms of its sliding averages, $\bar{u}(x, t^{n+1})$. An evaluation of these sliding averages at particular grid points provides the approximate cell averages of the solution at the next time level.

The choice of $x = x_j$ in (2.1) results in an upwind scheme. The solution then may be nonsmooth in the neighborhood of the points $\{x_{j+\frac{1}{2}}\}$, and the evaluation of the flux integrals in (2.1) requires the use of a computationally expensive (approximate) Riemann solver and characteristic decomposition.

If $x = x_{j+\frac{1}{2}}$ in (2.1), we obtain Godunov-type central schemes, namely,

$$\begin{aligned}\bar{u}_{j+\frac{1}{2}}^{n+1} = {} & \frac{1}{\Delta x}\left[\int_{x_j}^{x_{j+\frac{1}{2}}} p_j^n(x)\,dx + \int_{x_{j+\frac{1}{2}}}^{x_{j+1}} p_{j+1}^n(x)\,dx\right] \\ & -\frac{\lambda}{\Delta t}\left[\int_{t^n}^{t^{n+1}} f(u(x_{j+1},t))\,dt - \int_{t^n}^{t^{n+1}} f(u(x_j,t))\,dt\right], \quad \lambda := \frac{\Delta t}{\Delta x}.\end{aligned} \tag{2.4}$$

In contrast to the upwind framework, the solution is smooth in the neighborhood of the points $\{x_j\}$. Therefore, a discretization of the flux integrals in (2.4) can be done, using an appropriate quadrature formula. The corresponding function values can be computed either by Taylor expansion or by a Runge–Kutta method [39, 8].

2.2. Central schemes for Hamilton–Jacobi equations. In this section, we describe second-order Godunov-type central schemes for Hamilton–Jacobi equations. We follow the approach from [36] and construct a 1-D second-order staggered central scheme.

Assume that we have computed the point values of φ at time $t = t^n$. We then start with a continuous piecewise quadratic interpolant,

$$\begin{aligned}\widetilde{\varphi}(x, t^n) := {} & \varphi_j^n + \frac{(\Delta\varphi)_{j+\frac{1}{2}}^n}{\Delta x}(x - x_j) + \frac{(\Delta\varphi)'_{j+\frac{1}{2}}}{2(\Delta x)^2}(x - x_j)(x - x_{j+1}), \\ & x \in [x_j, x_{j+1}],\end{aligned} \tag{2.5}$$

where

$$(\Delta\varphi)_{j+\frac{1}{2}}^n := \varphi_{j+1}^n - \varphi_j^n. \tag{2.6}$$

Here, $(\Delta\varphi)'_{j+\frac{1}{2}}/(\Delta x)^2$ is an approximation to the second derivative $\varphi_{xx}(x_{j+\frac{1}{2}},t^n)$. An appropriate *nonlinear limiter* employed in this approximation guarantees the nonoscillatory nature of $\widetilde{\varphi}(x,t^n)$. Examples of such limiters, developed in the context of hyperbolic conservation laws, may be found in [15, 16, 23, 40, 43]. In this paper we use a one-parameter family of the *minmod* limiters [29, 15, 43]

$$(\Delta\varphi)'_{j+\frac{1}{2}}=\text{minmod}\Bigg(\theta\left[(\Delta\varphi)^n_{j+\frac{3}{2}}-(\Delta\varphi)^n_{j+\frac{1}{2}}\right],\frac{1}{2}\left[(\Delta\varphi)^n_{j+\frac{3}{2}}-(\Delta\varphi)^n_{j-\frac{1}{2}}\right],\\ \theta\left[(\Delta\varphi)^n_{j+\frac{1}{2}}-(\Delta\varphi)^n_{j-\frac{1}{2}}\right]\Bigg), \tag{2.7}$$

where $\theta\in[1,2]$, and the multivariable minmod function is defined by

$$\text{minmod}(x_1,x_2,\ldots):=\begin{cases}\min_j\{x_j\} & \text{if } x_j>0 \ \ \forall j,\\ \max_j\{x_j\} & \text{if } x_j<0 \ \ \forall j,\\ 0 & \text{otherwise.}\end{cases} \tag{2.8}$$

Notice that larger θ's in (2.7) correspond to less dissipative, but still *nonoscillatory* limiters [29, 15, 43].

Given a reconstruction (2.5), we consider the Hamilton–Jacobi equation (1.2), subject to the initial data $\varphi(x,0)=\widetilde{\varphi}(x,t^n)$. Under an appropriate CFL condition, due to the finite speed of propagation, the solution of this initial value problem is smooth in the neighborhood of the line segment $\{(x,t):\ x=x_{j+\frac{1}{2}},\ t^n\le t\le t^{n+1}\}$. Therefore, from the Taylor expansion of the solution about the point $(x_{j+\frac{1}{2}},t^n)$, we obtain

$$\varphi^{n+1}_{j+\frac{1}{2}}=\frac{\varphi^n_j+\varphi^n_{j+1}}{2}-\frac{(\Delta\varphi)'_{j+\frac{1}{2}}}{8}-\Delta tH\left(\frac{(\Delta\varphi)^n_{j+\frac{1}{2}}}{\Delta x}\right)+\frac{(\Delta t)^2}{2}\left[H'\left(\frac{(\Delta\varphi)^n_{j+\frac{1}{2}}}{\Delta x}\right)\right]^2\cdot\frac{(\Delta\varphi)'_{j+\frac{1}{2}}}{(\Delta x)^2}. \tag{2.9}$$

Remarks.

1. The derived scheme (2.9) is different from the one in [36]. There, the evolution step is executed by integration of (1.2) over $[t^n,t^{n+1}]$, followed by the application of the midpoint rule to the resulting integrals. For details, see [36, 27].
2. A 2-D staggered central scheme for (1.2) can be found in [36].

3. Central-upwind semidiscrete schemes. In this section, we develop new semidiscrete central-upwind schemes for conservation laws and Hamilton–Jacobi equations, following the approach presented in [26, 24, 25] and [27], respectively.

3.1. Semidiscrete central-upwind schemes for 1-D conservation laws. We consider the 1-D system (1.1) of N strictly hyperbolic conservation laws. We start with a piecewise polynomial reconstruction (2.3) with possible discontinuities at the interface points $\{x_{j+\frac{1}{2}}\}$. These discontinuities propagate with right- and left-sided local speeds, which can be estimated by

$$a^+_{j+\frac{1}{2}}:=\max_{\omega\in C\left(u^-_{j+\frac{1}{2}},u^+_{j+\frac{1}{2}}\right)}\left\{\lambda_N\Big(\frac{\partial f}{\partial u}(\omega)\Big),0\right\}$$

and

$$a^-_{j+\frac{1}{2}}:=\min_{\omega\in C\left(u^-_{j+\frac{1}{2}},u^+_{j+\frac{1}{2}}\right)}\left\{\lambda_1\Big(\frac{\partial f}{\partial u}(\omega)\Big),0\right\},$$

respectively. Here, $\lambda_1 < \cdots < \lambda_N$ are the N eigenvalues of the Jacobian $\frac{\partial f}{\partial u}$, and $C(u^-_{j+\frac12}, u^+_{j+\frac12})$ is the curve in the phase space that connects

$$u^+_{j+\frac12} := p_{j+1}(x_{j+\frac12}) \quad \text{and} \quad u^-_{j+\frac12} := p_j(x_{j+\frac12}). \tag{3.1}$$

For example, in the genuinely nonlinear or linearly degenerate case, we have

$$\begin{aligned} a^+_{j+\frac12} &= \max\left\{\lambda_N\Big(\frac{\partial f}{\partial u}\Big(u^-_{j+\frac12}\Big)\Big), \lambda_N\Big(\frac{\partial f}{\partial u}\Big(u^+_{j+\frac12}\Big)\Big), 0\right\},\\ a^-_{j+\frac12} &= \min\left\{\lambda_1\Big(\frac{\partial f}{\partial u}\Big(u^-_{j+\frac12}\Big)\Big), \lambda_1\Big(\frac{\partial f}{\partial u}\Big(u^+_{j+\frac12}\Big)\Big), 0\right\}. \end{aligned} \tag{3.2}$$

In fact, these one-sided local speeds are related to the CFL number. Note that in the schemes from [26, 24] only the spectral radius of $\frac{\partial f}{\partial u}$ is used, and for its computation one actually needs to know both λ_1 and λ_N.

Further, we utilize these one-sided local speeds of propagation in the following way. We consider the nonequal rectangular domains

$$[x^n_{j-\frac12,r}, x^n_{j+\frac12,l}] \times [t^n, t^{n+1}] \quad \text{and} \quad [x^n_{j+\frac12,l}, x^n_{j+\frac12,r}] \times [t^n, t^{n+1}], \tag{3.3}$$

with $x^n_{j+\frac12,l} := x_{j+\frac12} + \Delta t a^-_{j+\frac12}$ and $x^n_{j+\frac12,r} := x_{j+\frac12} + \Delta t a^+_{j+\frac12}$, where the solution of (1.1) with the initial data $\widetilde{u}(x, t^n)$ is smooth and nonsmooth, respectively.

The cell averages

$$\bar{w}^{n+1}_j = \frac{1}{x^n_{j+\frac12,l} - x^n_{j-\frac12,r}}\left[\int_{x^n_{j-\frac12,r}}^{x^n_{j+\frac12,l}} p^n_j(x)\,dx - \int_{t^n}^{t^{n+1}} \Big(f(u(x^n_{j+\frac12,l}, t)) - f(u(x^n_{j-\frac12,r}, t))\Big)\,dt\right], \tag{3.4}$$

and

$$\begin{aligned} \bar{w}^{n+1}_{j+\frac12} = \frac{1}{x^n_{j+\frac12,r} - x^n_{j+\frac12,l}}\Bigg[&\int_{x^n_{j+\frac12,l}}^{x_{j+\frac12}} p^n_j(x)\,dx + \int_{x_{j+\frac12}}^{x^n_{j+\frac12,r}} p^n_{j+1}(x)\,dx\\ &- \int_{t^n}^{t^{n+1}} \Big(f(u(x^n_{j+\frac12,r}, t)) - f(u(x^n_{j+\frac12,l}, t))\Big)\,dt\Bigg] \end{aligned} \tag{3.5}$$

are obtained by integrating (1.1) over the corresponding domains in (3.3); see Figure 3.1.

Given the polynomials $\{p^n_j\}$, the spatial integrals in (3.4) and (3.5) can be computed explicitly. To discretize the flux integrals there, one may use an appropriate quadrature formula, since the solution is smooth along the line segments $(x^n_{j+\frac12,l}, t)$, $t^n \le t < t^{n+1}$ and $(x^n_{j+\frac12,r}, t)$, $t^n \le t < t^{n+1}$.

Next, from the cell averages, $\bar{w}^{n+1}_{j+\frac12}$, $\bar{w}^{n+1}_j$, given by (3.4)–(3.5), we reconstruct a nonoscillatory, conservative, third-order, piecewise polynomial interpolant, denoted by

$$\widetilde{w}^{n+1}(x) = \sum_j \Big(\widetilde{w}^{n+1}_j(x)\chi_{\left[x^n_{j-\frac12,r},\, x^n_{j+\frac12,l}\right]} + \widetilde{w}^{n+1}_{j+\frac12}(x)\chi_{\left[x^n_{j+\frac12,l},\, x^n_{j+\frac12,r}\right]}\Big). \tag{3.6}$$

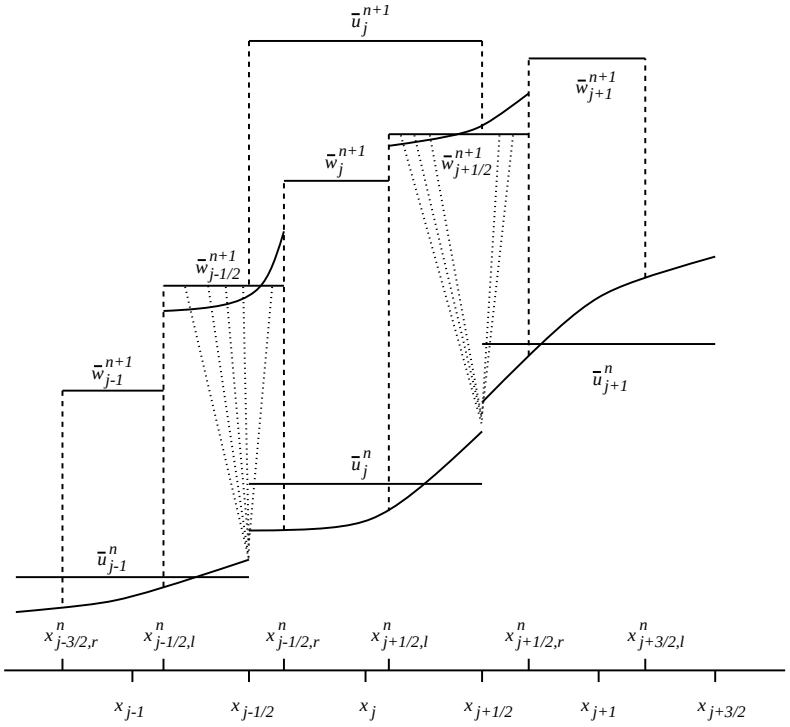

FIG. 3.1. *Central-upwind differencing.*

Here, the χ's are the characteristic functions, and $\{\widetilde{w}_{j+\frac{1}{2}}^{n+1}(x), \widetilde{w}_j^{n+1}(x)\}$ are the quadratic pieces, associated with the corresponding intervals. In fact, we do not need any high-order reconstruction $\widetilde{w}_j^{n+1}(x)$ since it will be averaged out (consult Figure 3.1).

Remark. Notice that even for a nonuniform grid, a particular piecewise quadratic reconstruction can be written explicitly. Since these formulae are rather messy and irrelevant for the semidiscrete scheme, we omit them.

The construction of our scheme is then completed by projecting $\widetilde{w}^{n+1}$ back onto the original grid, namely, we compute the cell averages

$$\bar{u}_j^{n+1} = \frac{1}{\Delta x}\int_{x_{j-\frac{1}{2}}}^{x_{j+\frac{1}{2}}} \widetilde{w}^{n+1}(x)\,dx \tag{3.7}$$

at the next time level. This leads to a fully discrete Godunov-type central-upwind scheme, which can be derived explicitly. Its derivation is similar to the derivation of the central schemes from [26, 24]. We omit here the details of these rather messy computations and continue within a much simpler semidiscrete framework.

The time derivative of $\bar{u}_j(t)$ is expressed with the help of (3.7) as

$$\frac{d}{dt}\bar{u}_j(t) = \lim_{\Delta t\to 0}\frac{\bar{u}_j^{n+1}-\bar{u}_j^n}{\Delta t} = \lim_{\Delta t\to 0}\frac{1}{\Delta t}\left[\frac{1}{\Delta x}\int_{x_{j-\frac{1}{2}}}^{x_{j+\frac{1}{2}}} \widetilde{w}^{n+1}(x)\,dx - \bar{u}_j^n\right]. \tag{3.8}$$

Now, let us suppose that the slopes of $\widetilde{w}_{j\pm\frac{1}{2}}^{n+1}$ are uniformly bounded, independently of

Δt. Since the width of the Riemann fans is bounded by $(a^+_{j+\frac12}-a^-_{j+\frac12})\Delta t$, we obtain

$$\widetilde{w}^{n+1}_{j\pm\frac12}(x)=\bar{w}^{n+1}_{j\pm\frac12}+\mathcal{O}(\Delta t)\qquad \forall x\in[x^n_{j\pm\frac12,l},\ x^n_{j\pm\frac12,r}]. \tag{3.9}$$

The conservation property of the reconstruction gives

$$\frac{1}{(x^n_{j+\frac12,l}-x^n_{j-\frac12,r})}\int_{x^n_{j-\frac12,r}}^{x^n_{j+\frac12,l}}\widetilde{w}^{n+1}_j(x)\,dx=\bar{w}^{n+1}_j. \tag{3.10}$$

From (3.8)–(3.10) and the definition of $x^n_{j-\frac12,r}$ and $x^n_{j+\frac12,l}$, we derive

$$\frac{d}{dt}\bar{u}_j(t)=\frac{a^+_{j-\frac12}}{\Delta x}\lim_{\Delta t\to0}\bar{w}^{n+1}_{j-\frac12}+\lim_{\Delta t\to0}\frac{1}{\Delta t}\left(\frac{x^n_{j+\frac12,l}-x^n_{j-\frac12,r}}{\Delta x}\bar{w}^{n+1}_j-\bar{u}^n_j\right)-\frac{a^-_{j+\frac12}}{\Delta x}\lim_{\Delta t\to0}\bar{w}^{n+1}_{j+\frac12}. \tag{3.11}$$

The three limits in (3.11) are computed separately. Using (3.4) and (3.5), we obtain

$$\lim_{\Delta t\to0}\frac{1}{\Delta t}\left(\frac{x^n_{j+\frac12,l}-x^n_{j-\frac12,r}}{\Delta x}\bar{w}^{n+1}_j-\bar{u}^n_j\right)=\frac{a^-_{j+\frac12}u^-_{j+\frac12}-a^+_{j-\frac12}u^+_{j-\frac12}}{\Delta x}-\frac{f(u^-_{j+\frac12})-f(u^+_{j-\frac12})}{\Delta x}, \tag{3.12}$$

and

$$\lim_{\Delta t\to0}\bar{w}^{n+1}_{j+\frac12}=\frac{a^+_{j+\frac12}u^+_{j+\frac12}-a^-_{j+\frac12}u^-_{j+\frac12}}{a^+_{j+\frac12}-a^-_{j+\frac12}}-\frac{f(u^+_{j+\frac12})-f(u^-_{j+\frac12})}{a^+_{j+\frac12}-a^-_{j+\frac12}}, \tag{3.13}$$

where, similarly to (3.1), $u^\pm_{j+\frac12}$ stand for the corresponding right and left values of the piecewise polynomial interpolant $\{p_j\}$, reconstructed at time t.

Finally, a substitution of (3.12) and (3.13) in (3.11) results in our new semidiscrete central-upwind scheme, which can be written in the following conservative form:

$$\frac{d}{dt}\bar{u}_j(t)=-\frac{H_{j+\frac12}(t)-H_{j-\frac12}(t)}{\Delta x}. \tag{3.14}$$

Here, the numerical fluxes $H_{j+\frac12}$ are given by

$$H_{j+\frac12}(t):=\frac{a^+_{j+\frac12}f(u^-_{j+\frac12})-a^-_{j+\frac12}f(u^+_{j+\frac12})}{a^+_{j+\frac12}-a^-_{j+\frac12}}+\frac{a^+_{j+\frac12}a^-_{j+\frac12}}{a^+_{j+\frac12}-a^-_{j+\frac12}}\left[u^+_{j+\frac12}-u^-_{j+\frac12}\right]. \tag{3.15}$$

Remarks.

1. The new semidiscrete scheme (3.14)–(3.15) is a Godunov-type central scheme, since it is based on integration over Riemann fans. It does not require characteristic decompositions and Riemann solvers, and therefore it preserves the main advantage of the central schemes—simplicity.
2. As with the semidiscrete schemes, proposed in [26], the numerical viscosity of (3.14)–(3.15) is independent of $\mathcal{O}(1/\Delta t)$, and thus it can be used for steady-state computations. Moreover, due to a more accurate estimate of the widths of the Riemann fans, the numerical dissipation in (3.14)–(3.15) is even smaller than the numerical viscosity of the schemes from [26, 24]. Notice that if

one takes $a^+_{j+\frac12} = -a^-_{j+\frac12} = a_{j+\frac12} := \max_{\omega\in C(u^{n-}_{j+\frac12},u^{n+}_{j+\frac12})} \rho(\frac{\partial f}{\partial u}(\omega))$, then the numerical flux (3.15) reduces to

$$H_{j+\frac12}(t) := \frac{f(u^+_{j+\frac12}) + f(u^-_{j+\frac12})}{2} - \frac{a_{j+\frac12}}{2}\left[u^+_{j+\frac12} - u^-_{j+\frac12}\right],$$

which is the numerical flux of the schemes from [26, 24].

3. We would like to point out that the first-order version of our scheme is exactly the semidiscrete version of the scheme in [17, 12]. Moreover, if the flux f is monotone, it reduces to the standard upwind scheme. That is why we call our new schemes *central-upwind*. For example, if $f'(u) \ge 0$, then $a^-_{j+\frac12} = 0$ $\forall j$, and the first-order scheme simplifies to
$$\dot u_j(t) = -\frac{f(u^n_j) - f(u^n_{j-1})}{\Delta x}.$$
4. A fully discrete, 2-D, third-order accurate scheme using the Harten–Lax–van Leer approximate Riemann solver [17, 12] was implemented and tested in [41].
5. It can be proved that a scalar second-order version of (3.14)–(3.15), together with the minmod reconstruction,
$$\begin{aligned}&\widetilde u^n_j(x) = \bar u^n_j + s^n_j(x - x_j),\\ &s^n_j = \operatorname{minmod}\left(\theta\frac{\bar u^n_j - \bar u^n_{j-1}}{\Delta x}, \frac{\bar u^n_{j+1} - \bar u^n_{j-1}}{2\Delta x}, \theta\frac{\bar u^n_{j+1} - \bar u^n_j}{\Delta x}\right),\end{aligned} \tag{3.16}$$
is a TVD scheme (for $1 \le \theta \le 2$), that is, $\|u(\cdot,t)\|_{BV} \le \|u(\cdot,0)\|_{BV}$. The proof is analogous to the proof of Theorem 4.1 in [26], and we leave the details to the reader.
6. The semidiscrete scheme (3.14)–(3.15) is a system of time-dependent ODEs, which can be solved by any stable ODE solver which retains the spatial accuracy of the semidiscrete scheme. In the numerical examples below, we have used the TVD Runge–Kutta method, proposed in [47, 45].
7. The scheme (3.14)–(3.15) can be easily generalized and applied to convection-diffusion equations in a straightforward manner. For details, we refer the reader to [26, 24].

3.2. Semidiscrete central-upwind schemes for multi-D conservation laws. The semidiscrete central-upwind schemes, presented in section 3.1, can be generalized to the multi-D case. Without loss of generality, we consider the 2-D system

$$u_t + f(u)_x + g(u)_y = 0. \tag{3.17}$$

Given the grid points $x_j := j\Delta x$, $y_k := k\Delta y$ and the intermediate points $x_{j\pm\frac12} := x_j \pm \frac{\Delta x}{2}$, $y_{k\pm\frac12} := y_k \pm \frac{\Delta y}{2}$, we start at time $t = t^n$ with a conservative piecewise polynomial reconstruction of an appropriate order:

$$\widetilde u^n(x,y) := \sum_{j,k} p^n_{j,k}(x,y)\chi_{j,k},$$

where $\chi_{j,k}$ is the characteristic function of the cell $[x_{j-\frac12}, x_{j+\frac12}] \times [y_{k-\frac12}, y_{k+\frac12}]$. In the numerical examples in this paper, we have used the third-order piecewise quadratic reconstruction, described in [25].

We use the notation

$$u_{j,k} := p^n_{j,k}(x_j, y_k), \quad u^{\rm N}_{j,k} := p^n_{j,k}(x_j, y_{k+\frac12}), \quad u^{\rm S}_{j,k} := p^n_{j,k}(x_j, y_{k-\frac12}),$$

$$u^{\rm E}_{j,k} := p^n_{j,k}(x_{j+\frac12}, y_k), \quad u^{\rm W}_{j,k} := p^n_{j,k}(x_{j-\frac12}, y_k), \quad u^{\rm NE}_{j,k} := p^n_{j,k}(x_{j+\frac12}, y_{k+\frac12}), \tag{3.18}$$

$$u^{\rm NW}_{j,k} := p^n_{j,k}(x_{j-\frac12}, y_{k+\frac12}), \quad u^{\rm SE}_{j,k} := p^n_{j,k}(x_{j+\frac12}, y_{k-\frac12}), \quad u^{\rm SW}_{j,k} := p^n_{j,k}(x_{j-\frac12}, y_{k-\frac12})$$

for the corresponding point values and

$$\bar u_{j,k} := \frac{1}{\Delta x\Delta y}\int_{x_{j-\frac12}}^{x_{j+\frac12}}\int_{y_{k-\frac12}}^{y_{k+\frac12}} p^n_{j,k}(x,y)\,dx\,dy$$

for the cell averages.

The piecewise polynomial interpolant $\widetilde u^n$ may have discontinuities along the lines $x = x_{j\pm\frac12}$ and $y = y_{k\pm\frac12}$, which propagate with different right- and left-sided local speeds. To estimate them is a nontrivial problem, but in practice one may use

$$\begin{aligned}
a^+_{j+\frac12,k} &:= \max\Big\{\lambda_N\Big(\frac{\partial f}{\partial u}(u^{\rm W}_{j+1,k})\Big), \lambda_N\Big(\frac{\partial f}{\partial u}(u^{\rm E}_{j,k})\Big), 0\Big\},\\
b^+_{j,k+\frac12} &:= \max\Big\{\lambda_N\Big(\frac{\partial g}{\partial u}(u^{\rm S}_{j,k+1})\Big), \lambda_N\Big(\frac{\partial g}{\partial u}(u^{\rm N}_{j,k})\Big), 0\Big\},\\
a^-_{j+\frac12,k} &:= \min\Big\{\lambda_1\Big(\frac{\partial f}{\partial u}(u^{\rm W}_{j+1,k})\Big), \lambda_1\Big(\frac{\partial f}{\partial u}(u^{\rm E}_{j,k})\Big), 0\Big\},\\
b^-_{j,k+\frac12} &:= \min\Big\{\lambda_1\Big(\frac{\partial g}{\partial u}(u^{\rm S}_{j,k+1})\Big), \lambda_1\Big(\frac{\partial g}{\partial u}(u^{\rm N}_{j,k})\Big), 0\Big\},
\end{aligned} \tag{3.19}$$

respectively. As in [25], we consider the nonuniform domains, outlined in Figure 3.2 and defined by

$$D_{j,k+\frac12} := [x_{j-\frac12}+A^+_{j-\frac12,k+\frac12}\Delta t,\ x_{j+\frac12}+A^-_{j+\frac12,k+\frac12}\Delta t]\times[y_{k+\frac12}+b^-_{j,k+\frac12}\Delta t,\ y_{k+\frac12}+b^+_{j,k+\frac12}\Delta t],$$

$$D_{j+\frac12,k} := [x_{j+\frac12}+a^-_{j+\frac12,k}\Delta t,\ x_{j+\frac12}+a^+_{j+\frac12,k}\Delta t]\times[y_{k-\frac12}+B^+_{j+\frac12,k-\frac12}\Delta t,\ y_{k+\frac12}+B^-_{j+\frac12,k+\frac12}\Delta t],$$

$$\begin{aligned}
D_{j+\frac12,k+\frac12} := [&x_{j+\frac12} + A^-_{j+\frac12,k+\frac12}\Delta t,\ x_{j+\frac12} + A^+_{j+\frac12,k+\frac12}\Delta t]\\
&\times[y_{k+\frac12} + B^-_{j+\frac12,k+\frac12}\Delta t,\ y_{k+\frac12} + B^+_{j+\frac12,k+\frac12}\Delta t],
\end{aligned}$$

$$D_{j,k} := [x_{j-\frac12},\ x_{j+\frac12}]\times[y_{k-\frac12},\ y_{k+\frac12}]\ \setminus\ \bigcup_{\pm}[D_{j,k\pm\frac12}\cup D_{j\pm\frac12,k}\cup D_{j\pm\frac12,k\pm\frac12}],$$

where

$$A^+_{j+\frac12,k+\frac12} := \max\Big\{a^+_{j+\frac12,k}, a^+_{j+\frac12,k+1}\Big\}, \qquad B^+_{j+\frac12,k+\frac12} := \max\Big\{b^+_{j,k+\frac12}, b^+_{j+1,k+\frac12}\Big\},$$

$$A^-_{j+\frac12,k+\frac12} := \min\Big\{a^-_{j+\frac12,k}, a^-_{j+\frac12,k+1}\Big\}, \qquad B^-_{j+\frac12,k+\frac12} := \min\Big\{b^-_{j,k+\frac12}, b^-_{j+1,k+\frac12}\Big\}.$$

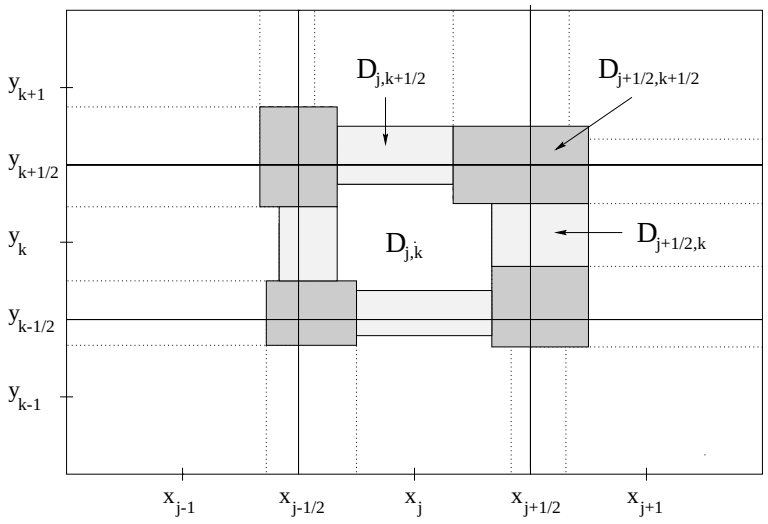

FIG. 3.2. 2-*D central-upwind differencing.*

Similarly to the 1-D case, under an appropriate CFL condition, the solution of system (3.17) with initial data $\widetilde{u}(x,y)$ is smooth in the domain $D_{j,k}$ and may be nonsmooth in the other domains. Notice that, in general, $D_{j,k}$ is a nonrectangular domain inside the (j,k)-cell; see Figure 3.2.

An integration of the system (3.17) over the domains

$$D_{j,k}\times[t^n,t^{n+1}],\quad D_{j\pm\frac12,k}\times[t^n,t^{n+1}],\ D_{j,k\pm\frac12}\times[t^n,t^{n+1}],\ D_{j\pm\frac12,k\pm\frac12}\times[t^n,t^{n+1}]$$

results in new cell averages $\{\bar{w}^{n+1}_{j,k+\frac12}\}$, $\{\bar{w}^{n+1}_{j+\frac12,k}\}$, $\{\bar{w}^{n+1}_{j+\frac12,k+\frac12}\}$, and $\{\bar{w}^{n+1}_{j,k}\}$. They are used for an intermediate piecewise polynomial reconstruction,

$$\widetilde{w}^{n+1}(x,y):=\sum_{j,k}\left[\widetilde{w}^{n+1}_{j,k}\widetilde{\chi}_{j,k}+\widetilde{w}^{n+1}_{j+\frac12,k}\widetilde{\chi}_{j+\frac12,k}+\widetilde{w}^{n+1}_{j,k+\frac12}\widetilde{\chi}_{j,k+\frac12}+\widetilde{w}^{n+1}_{j+\frac12,k+\frac12}\widetilde{\chi}_{j+\frac12,k+\frac12}\right]. \tag{3.20}$$

Here, similarly to (3.6), $\{\widetilde{w}^{n+1}_{j,k}(x,y),\widetilde{w}^{n+1}_{j+\frac12,k}(x,y),\widetilde{w}^{n+1}_{j,k+\frac12}(x,y),\widetilde{w}^{n+1}_{j+\frac12,k+\frac12}(x,y)\}$ are the quadratic pieces, and the $\widetilde{\chi}$'s stand for the characteristic functions of the corresponding domains D.

The construction of our 2-D fully discrete central-upwind scheme is then completed by projecting the interpolant (3.20) back onto the original cells,

$$\bar{u}^{n+1}_{j,k}=\frac{1}{\Delta x\Delta y}\int_{x_{j-\frac12}}^{x_{j+\frac12}}\int_{y_{k-\frac12}}^{y_{k+\frac12}}\widetilde{w}^{n+1}(x,y)\,dxdy. \tag{3.21}$$

The derivation of the explicit form of the fully discrete higher-order scheme is omitted, since it is rather complicated and is of no practical use. Note, however, that Wendroff [50] has recently proposed a 2-D version of the Harten–Lax–van Leer Riemann solver, which is closely related to the first-order fully discrete version of our scheme.

As in [25, section 3.3], we continue within the semidiscrete framework (as $\Delta t\to 0$), where all the computations are much simpler.

We use the following notation for the intersections of the cell $[x_{j-\frac12},x_{j+\frac12}]\times[y_{k-\frac12},y_{k+\frac12}]$ with the domains D – $C_{j\pm\frac12,k\pm\frac12}$ for the four corners, $S_{j\pm\frac12,k}$, $S_{j,k\pm\frac12}$ for the four side domains, and $D_{j,k}$ for the center. The sizes of these domains are $|C|\sim(\Delta t)^2$ and $|S|\sim\Delta t$. Since we assume that the spatial derivatives of $\widetilde{w}^{n+1}$ are bounded independently of Δt, the relation between $\widetilde{w}^{n+1}$ and $\bar{w}^{n+1}$ is given by

$$\int\int_{C_{j\pm\frac12,k\pm\frac12}}\widetilde{w}^{n+1}_{j\pm\frac12,k\pm\frac12}\,dxdy=\mathcal{O}((\Delta t)^2), \tag{3.22}$$

$$\int\int_{S_{j\pm\frac12,k}}\widetilde{w}^{n+1}_{j\pm\frac12,k}\,dxdy=|S_{j\pm\frac12,k}|\,\bar{w}^{n+1}_{j\pm\frac12,k}+\mathcal{O}(\Delta t^2), \tag{3.23}$$

$$\int\int_{S_{j,k\pm\frac12}}\widetilde{w}^{n+1}_{j,k\pm\frac12}\,dxdy=|S_{j,k\pm\frac12}|\,\bar{w}^{n+1}_{j,k\pm\frac12}+\mathcal{O}(\Delta t^2). \tag{3.24}$$

Also, the conservation property of the reconstruction $\widetilde{w}^{n+1}$ yields

$$\int\int_{D_{j,k}}\widetilde{w}^{n+1}_{j,k}(x,y)\,dxdy=|D_{j,k}|\bar{w}^{n+1}_{j,k}. \tag{3.25}$$

We now use (3.21) together with (3.22)–(3.25) and obtain

$$\begin{aligned}\frac{d}{dt}\bar{u}_{j,k}(t)&=\lim_{\Delta t\to0}\frac{\bar{u}^{n+1}_{j,k}-\bar{u}^{n}_{j,k}}{\Delta t}\\&=\lim_{\Delta t\to0}\left(\sum_{\pm}\frac{|S_{j,k\pm\frac12}|}{\Delta t\Delta x\Delta y}\bar{w}^{n+1}_{j,k\pm\frac12}+\sum_{\pm}\frac{|S_{j\pm\frac12,k}|}{\Delta t\Delta x\Delta y}\bar{w}^{n+1}_{j\pm\frac12,k}\right)\\&\quad+\lim_{\Delta t\to0}\frac{1}{\Delta t}\left[\frac{|D_{j,k}|}{\Delta x\Delta y}\bar{w}^{n+1}_{j,k}-\bar{u}^{n}_{j,k}\right].\end{aligned} \tag{3.26}$$

For the first sum on the right-hand side (RHS), we apply Simpson's quadrature formula to the integrals over $D_{j,k\pm\frac12}$ in the computation of $\bar{w}^{n+1}_{j,k\pm\frac12}$. Since $|S_{j,k\pm\frac12}|=\mp b^{\mp}_{j,k\pm\frac12}\Delta t\Delta x+\mathcal{O}((\Delta t)^2)$, we arrive at (consult [25] for details)

$$\begin{aligned}\lim_{\Delta t\to0}\frac{|S_{j,k\pm\frac12}|}{\Delta t\Delta x\Delta y}\bar{w}^{n+1}_{j,k\pm\frac12}\approx&-\frac{b^{+}_{j,k\pm\frac12}b^{-}_{j,k\pm\frac12}}{6\Big(b^{+}_{j,k\pm\frac12}-b^{-}_{j,k\pm\frac12}\Big)\Delta y}\left[u^{\mathrm{SW(NW)}}_{j,k\pm1}+4u^{\mathrm{S(N)}}_{j,k\pm1}+u^{\mathrm{SE(NE)}}_{j,k\pm1}\right]\\&+\frac{\Big(b^{\mp}_{j,k\pm\frac12}\Big)^2}{6\Big(b^{+}_{j,k\pm\frac12}-b^{-}_{j,k\pm\frac12}\Big)\Delta y}\left[u^{\mathrm{NW(SW)}}_{j,k}+4u^{\mathrm{N(S)}}_{j,k}+u^{\mathrm{NE(SE)}}_{j,k}\right]\\&+\frac{b^{\mp}_{j,k\pm\frac12}}{6\Big(b^{+}_{j,k\pm\frac12}-b^{-}_{j,k\pm\frac12}\Big)\Delta y}\Bigg[g(u^{\mathrm{SW(NW)}}_{j,k\pm1})-g(u^{\mathrm{NW(SW)}}_{j,k})\\&+4\Big(g(u^{\mathrm{S(N)}}_{j,k\pm1})-g(u^{\mathrm{N(S)}}_{j,k})\Big)+g(u^{\mathrm{SE(NE)}}_{j,k\pm1})-g(u^{\mathrm{NE(SE)}}_{j,k})\Bigg].\end{aligned} \tag{3.27}$$

The second sum on the RHS of (3.26) is treated similarly, and we obtain

$$\begin{aligned}\lim_{\Delta t\to 0}\frac{|S_{j\pm\frac12,k}|}{\Delta t\Delta x\Delta y}\bar w^{n+1}_{j\pm\frac12,k}\approx&-\frac{a^+_{j\pm\frac12,k}a^-_{j\pm\frac12,k}}{6\Big(a^+_{j\pm\frac12,k}-a^-_{j\pm\frac12,k}\Big)\Delta x}\Big[u^{\rm NW(NE)}_{j\pm1,k}+4u^{\rm W(E)}_{j\pm1,k}+u^{\rm SW(SE)}_{j\pm1,k}\Big]\\&+\frac{\Big(a^{\mp}_{j\pm\frac12,k}\Big)^2}{6\Big(a^+_{j\pm\frac12,k}-a^-_{j\pm\frac12,k}\Big)\Delta x}\Big[u^{\rm NE(NW)}_{j,k}+4u^{\rm E(W)}_{j,k}+u^{\rm SE(SW)}_{j,k}\Big]\\&+\frac{a^{\mp}_{j\pm\frac12,k}}{6\Big(a^+_{j\pm\frac12,k}-a^-_{j\pm\frac12,k}\Big)\Delta x}\Big[f(u^{\rm NW(NE)}_{j\pm1,k})-f(u^{\rm NE(NW)}_{j,k})\\&+4\Big(f(u^{\rm W(E)}_{j\pm1,k})-f(u^{\rm E(W)}_{j,k})\Big)f(u^{\rm SW(SE)}_{j\pm1,k})-f(u^{\rm SE(SW)}_{j,k})\Big].\end{aligned}\tag{3.28}$$

Finally, we consider the last term on the RHS of (3.26). Since the domain $D_{j,k}$ becomes *rectangular* as $\Delta t\to 0$, up to small corners of a negligible size $\mathcal{O}((\Delta t)^2)$, the integration of (3.17) over $D_{j,k}\times[t^n,t^n+\Delta t]$ and the application of Simpson's rule result in

$$\begin{aligned}\lim_{\Delta t\to 0}\frac{1}{\Delta t}&\left[\frac{|D_{j,k}|}{\Delta x\Delta y}\bar w^{n+1}_{j,k}-\bar u^n_{j,k}\right]\\&\approx\frac{a^-_{j+\frac12,k}}{6\Delta x}\Big[u^{\rm NE}_{j,k}+4u^{\rm E}_{j,k}+u^{\rm SE}_{j,k}\Big]-\frac{a^+_{j-\frac12,k}}{6\Delta x}\Big[u^{\rm NW}_{j,k}+4u^{\rm W}_{j,k}+u^{\rm SW}_{j,k}\Big]\\&+\frac{b^-_{j,k+\frac12}}{6\Delta y}\Big[u^{\rm NW}_{j,k}+4u^{\rm N}_{j,k}+u^{\rm NE}_{j,k}\Big]-\frac{b^+_{j,k-\frac12}}{6\Delta y}\Big[u^{\rm SW}_{j,k}+4u^{\rm S}_{j,k}+u^{\rm SE}_{j,k}\Big]\\&-\frac{1}{6\Delta x}\Big[f(u^{\rm NE}_{j,k})-f(u^{\rm NW}_{j,k})+4\Big(f(u^{\rm E}_{j,k})-f(u^{\rm W}_{j,k})\Big)+f(u^{\rm SE}_{j,k})-f(u^{\rm SW}_{j,k})\Big]\\&-\frac{1}{6\Delta y}\Big[g(u^{\rm NW}_{j,k})-g(u^{\rm SW}_{j,k})+4\Big(g(u^{\rm N}_{j,k})-g(u^{\rm S}_{j,k})\Big)+g(u^{\rm NE}_{j,k})-g(u^{\rm SE}_{j,k})\Big].\end{aligned}\tag{3.29}$$

Our 2-D semidiscrete central-upwind scheme is obtained by plugging (3.27)–(3.29) into (3.26). It can be written in the following conservative form:

$$\frac{d}{dt}\bar u_{j,k}(t)=-\frac{H^x_{j+\frac12,k}(t)-H^x_{j-\frac12,k}(t)}{\Delta x}-\frac{H^y_{j,k+\frac12}(t)-H^y_{j,k-\frac12}(t)}{\Delta y},\tag{3.30}$$

where the numerical fluxes are

$$\begin{aligned}H^x_{j+\frac12,k}:=&\frac{a^+_{j+\frac12,k}}{6\Big(a^+_{j+\frac12,k}-a^-_{j+\frac12,k}\Big)}\Big[f(u^{\rm NE}_{j,k})+4f(u^{\rm E}_{j,k})+f(u^{\rm SE}_{j,k})\Big]\\&-\frac{a^-_{j+\frac12,k}}{6\Big(a^+_{j+\frac12,k}-a^-_{j+\frac12,k}\Big)}\Big[f(u^{\rm NW}_{j+1,k})+4f(u^{\rm W}_{j+1,k})+f(u^{\rm SW}_{j+1,k})\Big]\\&+\frac{a^+_{j+\frac12,k}a^-_{j+\frac12,k}}{6\Big(a^+_{j+\frac12,k}-a^-_{j+\frac12,k}\Big)}\Big[u^{\rm NW}_{j+1,k}-u^{\rm NE}_{j,k}+4(u^{\rm W}_{j+1,k}-u^{\rm E}_{j,k})+u^{\rm SW}_{j+1,k}-u^{\rm SE}_{j,k}\Big]\end{aligned}\tag{3.31}$$

and

$$
\begin{aligned}
H^y_{j,k+\frac12} :=& \frac{b^+_{j,k+\frac12}}{6\Big(b^+_{j,k+\frac12}-b^-_{j,k+\frac12}\Big)}\Big[g(u^{\rm NW}_{j,k})+4g(u^{\rm N}_{j,k})+g(u^{\rm NE}_{j,k})\Big]\\
&-\frac{b^-_{j,k+\frac12}}{6\Big(b^+_{j,k+\frac12}-b^-_{j,k+\frac12}\Big)}\Big[g(u^{\rm SW}_{j,k+1})+4g(u^{\rm S}_{j,k+1})+g(u^{\rm SE}_{j,k+1})\Big]\\
&+\frac{b^+_{j,k+\frac12}b^-_{j,k+\frac12}}{6\Big(b^+_{j,k+\frac12}-b^-_{j,k+\frac12}\Big)}\Big[u^{\rm SW}_{j,k+1}-u^{\rm NW}_{j,k}+4(u^{\rm S}_{j,k+1}-u^{\rm N}_{j,k})+u^{\rm SE}_{j,k+1}-u^{\rm NE}_{j,k}\Big].
\end{aligned}
\tag{3.32}
$$

Here, the one-sided local speeds $a^\pm_{j+\frac12,k}, b^\pm_{j,k+\frac12}$ are defined in (3.19), and the values of the u's are computed in (3.18), using the piecewise quadratic reconstruction $\{p_{j,k}\}$ at time t. In our numerical examples, we have implemented the reconstruction introduced in [25].

Remarks.

1. Our 2-D semidiscrete central-upwind scheme (3.30)–(3.32) is a Godunov-type *central* scheme; therefore it can be applied *componentwise* and does not require Riemann solvers. As in [25], this scheme is constructed as a genuinely multi-D scheme. Moreover, if one sets

$$
\begin{aligned}
a^+_{j+\frac12,k} &:= -a^-_{j+\frac12,k} := \max\Big\{a^+_{j+\frac12,k},-a^-_{j+\frac12,k}\Big\},\\
b^+_{j,k+\frac12} &:= -b^-_{j,k+\frac12} := \max\Big\{b^+_{j,k+\frac12},-b^-_{j,k+\frac12}\Big\},
\end{aligned}
$$

   the scheme (3.30)–(3.32) reduces to the one in [25].

2. As in the 1-D case, our 2-D scheme (3.30)–(3.32) has an upwind nature. To illustrate this, let us consider the simplest linear scalar advection equation, $u_t+au_x+bu_y=0$, with positive a and b. In this setting, the first-order version of the scheme (3.30)–(3.32) becomes a standard first-order upwind scheme

$$
\frac{d}{dt}u_{j,k}(t)=-a\frac{u_{j,k}-u_{j-1,k}}{\Delta x}-b\frac{u_{j,k}-u_{j,k-1}}{\Delta y}.
$$

3. A second-order version of the 2-D scheme (3.30)–(3.32) can be obtained if one uses a second-order piecewise polynomial reconstruction (say, the minmod reconstruction) and a lower-order midpoint quadrature instead of the fourth-order Simpson's rule. This results in the scheme

$$
\frac{d}{dt}u_{j,k}(t)=-\frac{H^x_{j+\frac12,k}(t)-H^x_{j-\frac12,k}(t)}{\Delta x}-\frac{H^y_{j,k+\frac12}(t)-H^y_{j,k-\frac12}(t)}{\Delta y},
\tag{3.33}
$$

   with the corresponding numerical fluxes

$$
H^x_{j+\frac12,k} := \frac{a^+_{j+\frac12,k}f(u^{\rm E}_{j,k})-a^-_{j+\frac12,k}f(u^{\rm W}_{j+1,k})}{a^+_{j+\frac12,k}-a^-_{j+\frac12,k}}+\frac{a^+_{j+\frac12,k}a^-_{j+\frac12,k}}{a^+_{j+\frac12,k}-a^-_{j+\frac12,k}}\Big[u^{\rm W}_{j+1,k}-u^{\rm E}_{j,k}\Big]
\tag{3.34}
$$

and

$$H^y_{j,k+\frac12}:=\frac{b^+_{j,k+\frac12}g(u^{\rm N}_{j,k})-b^-_{j,k+\frac12}g(u^{\rm S}_{j,k+1})}{b^+_{j,k+\frac12}-b^-_{j,k+\frac12}}+\frac{b^+_{j,k+\frac12}b^-_{j,k+\frac12}}{b^+_{j,k+\frac12}-b^-_{j,k+\frac12}}\Big[u^{\rm S}_{j,k+1}-u^{\rm N}_{j,k}\Big]. \tag{3.35}$$

The same scheme can also be derived by applying the 1-D numerical flux (3.15) in both x- and y-directions (this is the so-called dimension-by-dimension approach, used in [26]).

4. The scheme (3.30)–(3.32) can be generalized and applied to convection-diffusion equations (for details see [26, 25, 24]). Also, it can be rather easily extended to the multi-D case, $d \geq 3$.

3.2.1. Maximum principle for the second-order central-upwind scheme. We consider the 2-D second-order central-upwind scheme (3.33)–(3.35), together with the minmod reconstruction (3.16). We solve the time-dependent ODE system (3.33), using a TVD Runge–Kutta method. Under an appropriate CFL condition, the resulting fully discrete scheme, applied to a scalar conservation law, satisfies the maximum principle; see the following theorem.

THEOREM 3.1 (maximum principle). *Consider the scalar conservation laws* (3.17). *Then the second-order scheme* (3.33)–(3.35)*, with the minmod reconstruction* (3.16)*, coupled with a TVD Runge–Kutta method* [47, 45] *satisfies the maximum principle*

$$\min_{j,k}\{u^n_{j,k}\}\leq\min_{j,k}\{u^{n+1}_{j,k}\}\leq\max_{j,k}\{u^{n+1}_{j,k}\}\leq\max_{j,k}\{u^n_{j,k}\} \tag{3.36}$$

under the CFL condition

$$\max\left(\frac{\Delta t^n}{\Delta x}\max_u|f'(u)|,\frac{\Delta t^n}{\Delta y}\max_u|g'(u)|\right)\leq\frac18, \tag{3.37}$$

where Δt^n is the variable time step of the Runge–Kutta method.

We omit the proof since it is similar to the proof of Theorem 5.1 in [26].

3.3. Semidiscrete central-upwind scheme for Hamilton–Jacobi equations. In this section, we propose a new Godunov-type central-upwind scheme for the 1-D and 2-D Hamilton–Jacobi equations (1.2). We follow the approach in [27], but this time we utilize more precise information about the *one-sided* local speeds of propagation.

We begin with the 1-D case and start at time level $t = t^n$ with the continuous piecewise polynomial interpolant $\widetilde{\varphi}(x,t^n)$ and estimate the maximal one-sided local speeds, a^+_j and a^-_j. For example, in the convex case, they are equal to

$$a^+_j:=\max\{H'(\varphi^+_x),H'(\varphi^-_x),0\},\qquad a^-_j:=\min\{H'(\varphi^+_x),H'(\varphi^-_x),0\}, \tag{3.38}$$

where we use the notation $\varphi^\pm_x:=\widetilde{\varphi}_x(x_j\pm0,t^n)$. To construct the second-order scheme one should use the continuous piecewise quadratic polynomial (2.5), and in this case,

$$\varphi^\pm_x=\frac{(\Delta\varphi)^n_{j\pm\frac12}}{\Delta x}\mp\frac{(\Delta\varphi)'_{j\pm\frac12}}{2\Delta x}. \tag{3.39}$$

Note that under an appropriate CFL-condition, the solution of the Hamilton–Jacobi equation (1.2) with the piecewise polynomial initial data $\widetilde{\varphi}(x,t^n)$ is smooth

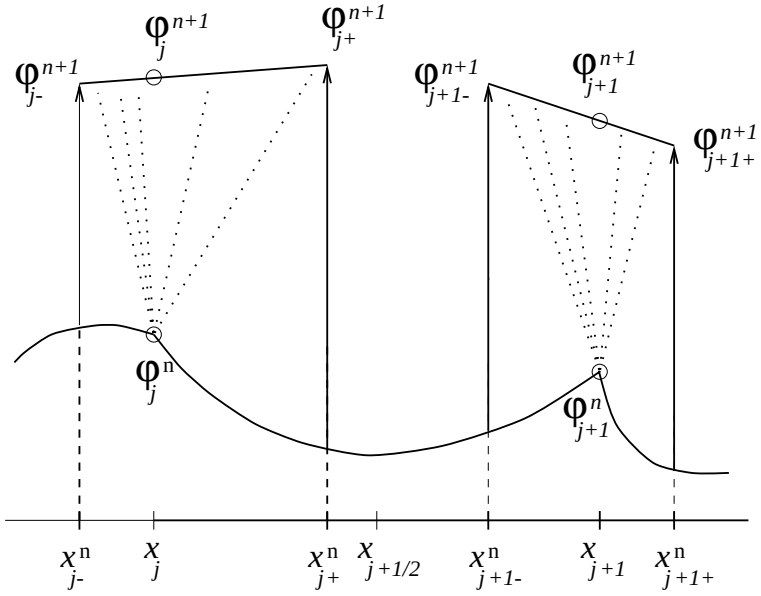

FIG. 3.3. *Central-upwind differencing*—1-D.

along the line segments $(x_{j\pm}^n, t)$, $t^n \le t < t^{n+1}$, $x_{j\pm}^n := x_j + a_j^{\pm}\Delta t$; see Figure 3.3. Therefore, one can use the Taylor expansion to compute the intermediate point values at the next time level:

$$\varphi_{j\pm}^{n+1} = \widetilde{\varphi}(x_{j\pm}, t^n) - \Delta t \cdot H(\widetilde{\varphi}_x(x_{j\pm}^n, t^n)) + \mathcal{O}(\Delta t)^2. \tag{3.40}$$

We complete the construction of our fully discrete central-upwind scheme by projecting the intermediate point values back onto the original grid. Since the distance between x_{j+}^n and x_{j-}^n is proportional to Δt, it suffices to compute the weighted averages of φ_{j+}^{n+1} and φ_{j-}^{n+1}, that is,

$$\varphi_j^{n+1} = \frac{a_j^+}{a_j^+ - a_j^-}\varphi_{j-}^{n+1} - \frac{a_j^-}{a_j^+ - a_j^-}\varphi_{j+}^{n+1} + \mathcal{O}(\Delta t)^2. \tag{3.41}$$

Finally, we substitute (3.40) in (3.41), and arrive at the fully discrete scheme

$$\begin{aligned}\varphi_j^{n+1} = {} & \frac{a_j^+}{a_j^+ - a_j^-}\Big(\widetilde{\varphi}(x_{j-}, t^n) - \Delta t H(\widetilde{\varphi}_x(x_{j-}^n, t^n))\Big) \\ & - \frac{a_j^-}{a_j^+ - a_j^-}\Big(\widetilde{\varphi}(x_{j+}, t^n) - \Delta t H(\widetilde{\varphi}_x(x_{j+}^n, t^n))\Big),\end{aligned} \tag{3.42}$$

which is high-order in space (depending on the order of the piecewise polynomial reconstruction) and only first-order in time.

A semidiscrete version of the scheme (3.42), coupled with a high-order ODE solver, will allow us to achieve high accuracy both in space and time. To derive such

a scheme, we first use the Taylor expansions, $\widetilde{\varphi}(x_{j\pm},t^n)=\widetilde{\varphi}(x_j,t^n)+\Delta t a_j^{\pm}\widetilde{\varphi}_x(x_j\pm 0,t^n)+\mathcal{O}(\Delta t)^2$, and rewrite the fully discrete scheme (3.42) as

$$\begin{aligned}\varphi_j^{n+1}=\varphi_j^n&-\Delta t\frac{a_j^+a_j^-}{a_j^+-a_j^-}\Big[\widetilde{\varphi}_x(x_j+0,t^n)-\widetilde{\varphi}_x(x_j-0,t^n)\Big]\\&+\frac{\Delta t}{a_j^+-a_j^-}\Big[a_j^-H(\widetilde{\varphi}_x(x_{j+}^n,t^n))-a_j^+H(\widetilde{\varphi}_x(x_{j-}^n,t^n))\Big]+\mathcal{O}(\Delta t)^2.\end{aligned}\tag{3.43}$$

We now let $\Delta t\to 0$, and end up with the following semidiscrete central-upwind scheme:

$$\frac{d}{dt}\varphi_j(t)=\frac{1}{a_j^+-a_j^-}\Big[a_j^-H(\varphi_x^+)-a_j^+H(\varphi_x^-)\Big]-\frac{a_j^+a_j^-}{a_j^+-a_j^-}\Big(\varphi_x^+-\varphi_x^-\Big).\tag{3.44}$$

Here, $a_j^{\pm}$ are given by (3.38), and $\varphi_x^{\pm}$ are the right and the left derivatives at the point $x=x_j$ of the reconstruction $\widetilde{\varphi}(\cdot,t)$ at time t.

We continue with the construction of a multi-D extension of the scheme (3.44). Without loss of generality, we consider the 2-D Hamilton–Jacobi equation,

$$\varphi_t+H(\varphi_x,\varphi_y)=0.\tag{3.45}$$

Assume that at time $t=t^n$ the discrete approximation to the point values of its solution, $\{\varphi_{j,k}^n\approx\varphi(x_j,y_k,t^n)\}$, has already been computed. We then construct the 2-D continuous piecewise polynomial interpolant $\widetilde{\varphi}(x,y,t^n)$. Such a reconstruction is defined over the four triangles (NW, NE, SW, and SE) around each grid-point (x_j,y_k) (see Figure 3.4). We refer the reader to [27] for an example of a nonoscillatory second-order piecewise quadratic interpolant.

We now continue with the construction of our semidiscrete central-upwind scheme. As in the 1-D case, we use the maximal values of the one-sided local speeds of propagation in the x- and y-directions. These values at the grid-point (x_j,y_k) are given by

$$\begin{aligned}&a_{j,k}^+:=\max_{C_{j,k}}\Big\{H_u(\widetilde{\varphi}_x(x,y),\widetilde{\varphi}_y(x,y))\Big\}_+,\quad a_{j,k}^-:=\min_{C_{j,k}}\Big\{H_u(\widetilde{\varphi}_x(x,y),\widetilde{\varphi}_y(x,y))\Big\}_-,\\&b_{j,k}^+:=\max_{C_{j,k}}\Big\{H_v(\widetilde{\varphi}_x(x,y),\widetilde{\varphi}_y(x,y))\Big\}_+,\quad b_{j,k}^-:=\min_{C_{j,k}}\Big\{H_v(\widetilde{\varphi}_x(x,y),\widetilde{\varphi}_y(x,y))\Big\}_-,\end{aligned}\tag{3.46}$$

where $C_{j,k}:=[x_{j-\frac12},x_{j+\frac12}]\times[y_{k-\frac12},y_{k+\frac12}]$ and $(\,\cdot\,)_+:=\max(\cdot,0)$, $(\,\cdot\,)_-:=\min(\cdot,0)$.

To compute the solution at the next time level $t=t^{n+1}$, we use the intermediate values $\{\varphi_{j\pm,k\pm}^{n+1}\}$, obtained by the Taylor expansion about the points ($x_{j\pm}^n:=x_j+a_{j,k}^{\pm}\Delta t$, $y_{k\pm}^n:=y_k+b_{j,k}^{\pm}\Delta t$),

$$\varphi_{j\pm,k\pm}^{n+1}=\widetilde{\varphi}(x_{j\pm}^n,y_{k\pm}^n,t^n)-\Delta t\cdot H(\widetilde{\varphi}_x(x_{j\pm}^n,y_{k\pm}^n,t^n),\widetilde{\varphi}_y(x_{j\pm}^n,y_{k\pm}^n,t^n))+\mathcal{O}(\Delta t)^2.\tag{3.47}$$

Expansion (3.47) is valid, since due to the finite speed of propagation, the solution of (3.45) with the initial data $\widetilde{\varphi}(x,y,t^n)$ is smooth around $(x_{j\pm}^n,y_{k\pm}^n)$; see Figure 3.4.

Next, the computed intermediate values (3.47) are projected back onto the original grid. This can be done using the weighted average of the values $\varphi_{j\pm,k\pm}^{n+1}$, since the

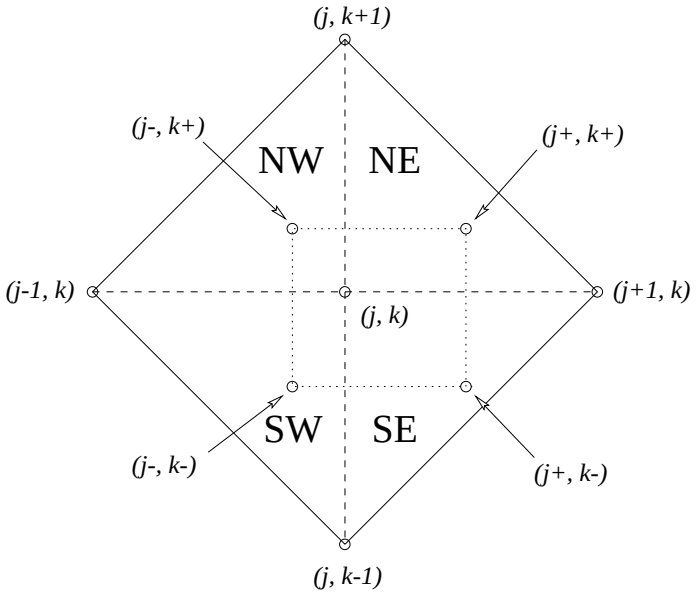

FIG. 3.4. *Central-upwind differencing*—2-D.

distance between the points $(x_{j\pm}, y_{k\pm})$ is proportional to $\mathcal{O}(\Delta t)$. The resulting fully discrete central-upwind scheme is

$$\begin{aligned}
&\varphi_{j,k}^{n+1}\\
&= \frac{a_{j,k}^- b_{j,k}^-}{(a_{j,k}^+ - a_{j,k}^-)(b_{j,k}^+ - b_{j,k}^-)}\Big(\widetilde{\varphi}(x_{j+}^n, y_{k+}^n, t^n) - \Delta t \cdot H(\widetilde{\varphi}_x(x_{j+}^n, y_{k+}^n, t^n), \widetilde{\varphi}_y(x_{j+}^n, y_{k+}^n, t^n))\Big)\\
&- \frac{a_{j,k}^- b_{j,k}^+}{(a_{j,k}^+ - a_{j,k}^-)(b_{j,k}^+ - b_{j,k}^-)}\Big(\widetilde{\varphi}(x_{j+}^n, y_{k-}^n, t^n) - \Delta t \cdot H(\widetilde{\varphi}_x(x_{j+}^n, y_{k-}^n, t^n), \widetilde{\varphi}_y(x_{j+}^n, y_{k-}^n, t^n))\Big)\\
&- \frac{a_{j,k}^+ b_{j,k}^-}{(a_{j,k}^+ - a_{j,k}^-)(b_{j,k}^+ - b_{j,k}^-)}\Big(\widetilde{\varphi}(x_{j-}^n, y_{k+}^n, t^n) - \Delta t \cdot H(\widetilde{\varphi}_x(x_{j-}^n, y_{k+}^n, t^n), \widetilde{\varphi}_y(x_{j-}^n, y_{k+}^n, t^n))\Big)\\
&+ \frac{a_{j,k}^+ b_{j,k}^+}{(a_{j,k}^+ - a_{j,k}^-)(b_{j,k}^+ - b_{j,k}^-)}\Big(\widetilde{\varphi}(x_{j-}^n, y_{k-}^n, t^n) - \Delta t \cdot H(\widetilde{\varphi}_x(x_{j-}^n, y_{k-}^n, t^n), \widetilde{\varphi}_y(x_{j-}^n, y_{k-}^n, t^n))\Big).
\end{aligned} \tag{3.48}$$

As in the 1-D case, the scheme (3.48) is only first-order in time. This disadvantage can be eliminated by passing to the semidiscrete limit in (3.48) as $\Delta t \to 0$. To this end, we first compute the values of $\widetilde{\varphi}(x_{\pm}^n, y_{\pm}^n, t^n)$ by the Taylor expansions,

$$\begin{aligned}
\widetilde{\varphi}(x_{j\pm}, y_{k+}, t^n) &= \widetilde{\varphi}(x_j, y_k, t^n) + \Delta t a_{j,k}^{\pm}\widetilde{\varphi}_x(x_j \pm 0, y_k, t^n)\\
&\quad + \Delta t b_{j,k}^+\widetilde{\varphi}_y(x_j, y_k + 0, t^n) + \mathcal{O}(\Delta t)^2,\\
\widetilde{\varphi}(x_{j\pm}, y_{k-}, t^n) &= \widetilde{\varphi}(x_j, y_k, t^n) + \Delta t a_{j,k}^{\pm}\widetilde{\varphi}_x(x_j \pm 0, y_k, t^n)\\
&\quad + \Delta t b_{j,k}^-\widetilde{\varphi}_y(x_j, y_k - 0, t^n) + \mathcal{O}(\Delta t)^2.
\end{aligned}$$

We then plug these values in (3.48), and after passing to the limit as $\Delta t \to 0$, we obtain the 2-*D semidiscrete central-upwind scheme*,

$$\frac{d}{dt}\varphi_{j,k}(t)$$
$$= -\frac{a^-_{j,k}b^-_{j,k}H(\varphi^+_x,\varphi^+_y) - a^-_{j,k}b^+_{j,k}H(\varphi^+_x,\varphi^-_y) - a^+_{j,k}b^-_{j,k}H(\varphi^-_x,\varphi^+_y) + a^+_{j,k}b^+_{j,k}H(\varphi^-_x,\varphi^-_y)}{(a^+_{j,k}-a^-_{j,k})(b^+_{j,k}-b^-_{j,k})}$$
$$-\frac{a^+_{j,k}a^-_{j,k}}{a^+_{j,k}-a^-_{j,k}}\Big(\varphi^+_x-\varphi^-_x\Big)-\frac{b^+_{j,k}b^-_{j,k}}{b^+_{j,k}-b^-_{j,k}}\Big(\varphi^+_y-\varphi^-_y\Big). \tag{3.49}$$

Here, $\varphi^\pm_x := \widetilde{\varphi}_x(x_j \pm 0, y_k, t)$ and $\varphi^\pm_y := \widetilde{\varphi}_y(x_j, y_k \pm 0, t)$ are the right and the left derivatives in the x- and y-direction, respectively. The one-sided local speeds in (3.49) are given by (3.46). In practice, these speeds can be estimated in a simpler way. For instance, in the numerical examples, we have used

$$a^+_{j,k} := \max_{\pm}\Big\{H_u(\varphi^\pm_x,\varphi^\pm_y)\Big\}_+, \quad a^-_{j,k} := \min_{\pm}\Big\{H_u(\varphi^\pm_x,\varphi^\pm_y)\Big\}_-,$$
$$b^+_{j,k} := \max_{\pm}\Big\{H_v(\varphi^\pm_x,\varphi^\pm_y)\Big\}_+, \quad b^-_{j,k} := \min_{\pm}\Big\{H_v(\varphi^\pm_x,\varphi^\pm_y)\Big\}_-. \tag{3.50}$$

Finally, to obtain the same second-order accuracy in time, our semidiscrete central-upwind scheme (3.49)–(3.50) should be complemented with at least a second-order ODE solver for time discretization.

4. Numerical examples. In this section, we implement our scheme for conservation laws and Hamilton–Jacobi equations and perform several numerical experiments. We test the accuracy of the scheme on problems with smooth solutions and solve various equations which admit nonsmooth solutions. Among them are the Euler equations of gas dynamics, the incompressible Euler equations, and others. The numerical results show that our scheme gives sharper resolution and reduces some of the side effects of the schemes from [27, 25].

The high-order semidiscrete methods, presented in this paper, require a time discretization of the corresponding order. In the numerical examples, shown below, we have used the third-order TVD Runge–Kutta method, proposed in [45, 47], and the second-order modified Euler method. Our choice is based on the stability properties of these methods, each time step of which can be viewed as a convex combination of small forward Euler steps.

In all the numerical experiments below, the CFL number is equal to 0.475, and the value of θ in the generalized minmod limiter is 2.

4.1. 1-D problems.

Example 1. Burgers' equation. We consider the initial boundary value problem (IBVP) for the inviscid Burgers' equation

$$u_t + \Big(\frac{u^2}{2}\Big)_x = 0, \qquad u(x,0) = 0.5 + \sin x, \quad x \in [0, 2\pi], \tag{4.1}$$

with periodic boundary conditions. It is known that the unique entropy solution of (4.1) develops a shock discontinuity at time $t = 1$. The solution at the preshock time $T = 0.5$ is smooth, and this allows us to test the accuracy of the 1-D third-order central-upwind scheme (3.14)–(3.15). We couple it with the basic piecewise quadratic reconstruction (for details, see [37, 39, 25]), and compute the solution using N grid points, $N = 40, 80, \ldots, 1280$.

The L^∞- and L^1-errors are shown in Table 4.1, and they clearly demonstrate a third-order experimental convergence rate.

TABLE 4.1
Accuracy test for the Burgers' equation (4.1), $T = 0.5$.

N	L^∞-error	rate	L^1-error	rate
40	1.456e-03	–	1.241e-03	–
80	2.177e-04	2.74	1.683e-04	2.88
160	2.893e-05	2.91	2.187e-05	2.94
320	3.689e-06	2.97	2.794e-06	2.97
640	4.559e-07	3.02	3.484e-07	3.00
1280	5.720e-08	2.99	4.376e-08	2.99

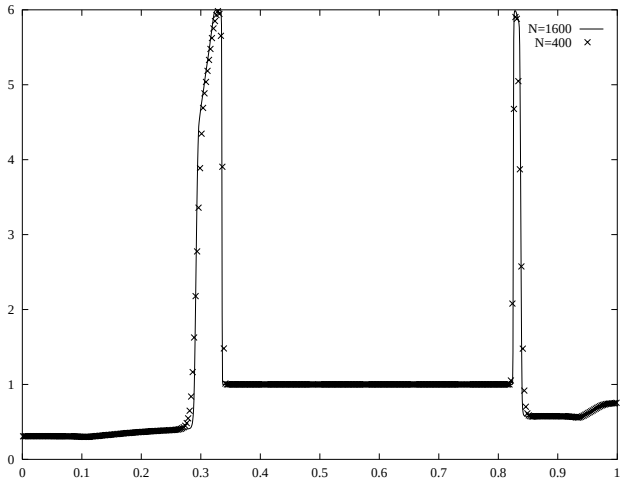

FIG. 4.1. *Problem* (4.2)–(4.3)*, density at* $T = 0.01$.

Example 2. 1-D Euler equations of gas dynamics. We solve the 1-D Euler system

$$\frac{\partial}{\partial t}\begin{bmatrix}\rho\\ m\\ E\end{bmatrix}+\frac{\partial}{\partial x}\begin{bmatrix}m\\ \rho u^2+p\\ u(E+p)\end{bmatrix}=0,\qquad p=(\gamma-1)\cdot\Big(E-\frac{\rho}{2}u^2\Big), \tag{4.2}$$

with the initial data

$$\vec{u}(x,0)=\begin{cases}\vec{u}_L=(1,0,2500)^T, & 0\le x<0.1,\\ \vec{u}_M=(1,0,0.025)^T, & 0.1\le x<0.9,\\ \vec{u}_R=(1,0,250)^T, & 0.9\le x<1,\end{cases} \tag{4.3}$$

and solid wall boundary conditions, applied to both ends. This problem, proposed in [51], models the interaction of blast waves. Here, ρ, u, $m=\rho u$, p, and E are the density, velocity, momentum, pressure, and the total energy, respectively; $\gamma = 1.4$.

The solution is computed with our scheme (3.14)–(3.15) and the 1-D reconstruction in [25]. We use $N = 400$ grid points and plot the density, the velocity, and the pressure together with a reference solution, obtained by the same method with $N = 1600$.

Figures 4.1, 4.2, and 4.3 show the density, the velocity, and the pressure at time $T = .01$. Note, that for $N = 400$, the second density spike has a height of ~ 5.9, which is closer to the actual value of the solution. This result is better than the heights of

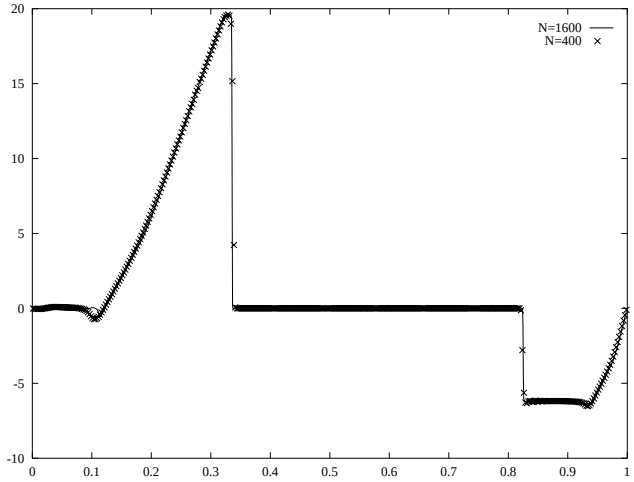

FIG. 4.2. *Problem* (4.2)–(4.3)*, velocity at* $T = 0.01$.

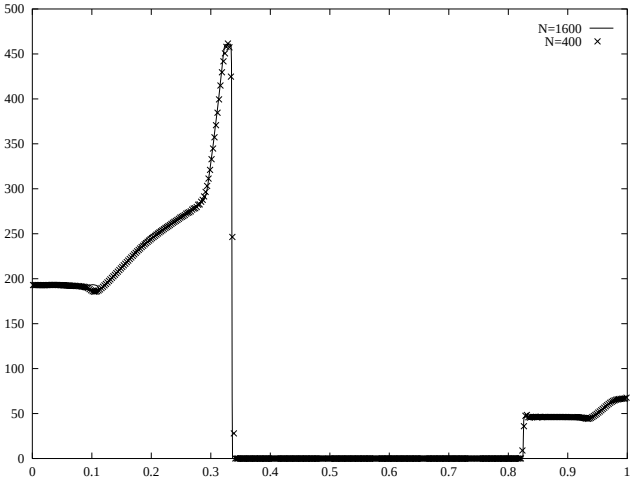

FIG. 4.3. *Problem* (4.2)–(4.3)*, pressure at* $T = 0.01$.

~ 5.75, ~ 5.2, and ~ 3.7, obtained by the third-order central schemes in [25, 39], and the second-order Nessyahu–Tadmor scheme in [40], respectively. This illustrates the higher resolution and smaller numerical dissipation of the central-upwind scheme.

The computations at times $T = 0.03$ and $T = 0.038$ are comparable to the results from [25], and are shown in Figures 4.4–4.9.

Example 3. 1-D Hamilton–Jacobi equation. In this example, we apply the second-order central-upwind scheme (2.7), (3.38)–(3.39), (3.44) to the Riemann problem for a 1-D Hamilton–Jacobi equation with a nonconvex Hamiltonian,

$$\varphi_t + \frac{1}{4}(\varphi_x^2 - 1)(\varphi_x^2 - 4) = 0, \qquad \varphi(x,0) = -2|x|. \tag{4.4}$$

The numerical solution, computed for different numbers of grid points is plotted in Figure 4.10. One can observe a very fast convergence of the approximate solutions

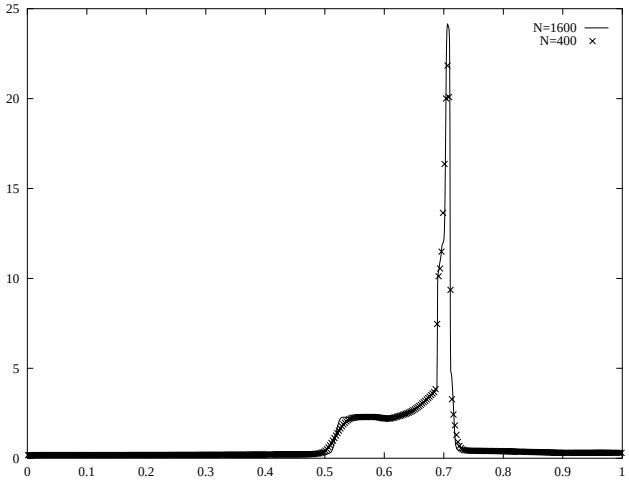

FIG. 4.4. *Problem* (4.2)–(4.3), *density at* $T = 0.03$.

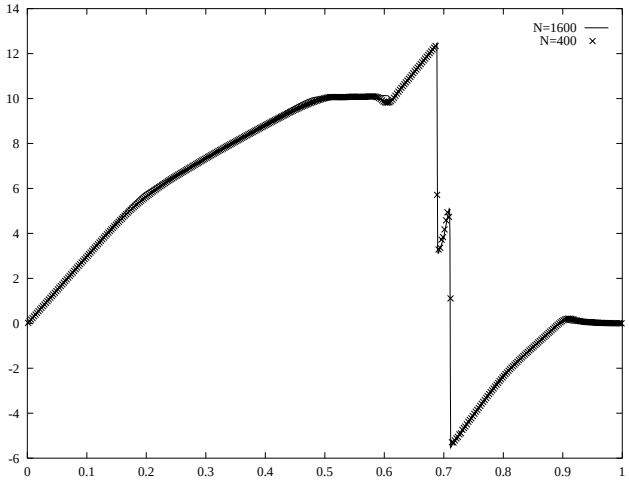

FIG. 4.5. *Problem* (4.2)–(4.3), *velocity at* $T = 0.03$.

toward the exact (viscosity) solution of (4.4) as the mesh is refined. The exact solution is obtained by solving the Riemann problem for the corresponding conservation law.

4.2. 2-D problems.

Example 4. 2-D Euler equations of gas dynamics. We solve the 2-D compressible Euler equations

$$\frac{\partial}{\partial t}\begin{bmatrix}\rho\\ \rho u\\ \rho v\\ E\end{bmatrix}+\frac{\partial}{\partial x}\begin{bmatrix}\rho u\\ \rho u^2+p\\ \rho uv\\ u(E+p)\end{bmatrix}+\frac{\partial}{\partial y}\begin{bmatrix}\rho v\\ \rho uv\\ \rho v^2+p\\ v(E+p)\end{bmatrix}=0,\ \ p=(\gamma-1)\cdot\Big[E-\frac{\rho}{2}(u^2+v^2)\Big] \tag{4.5}$$

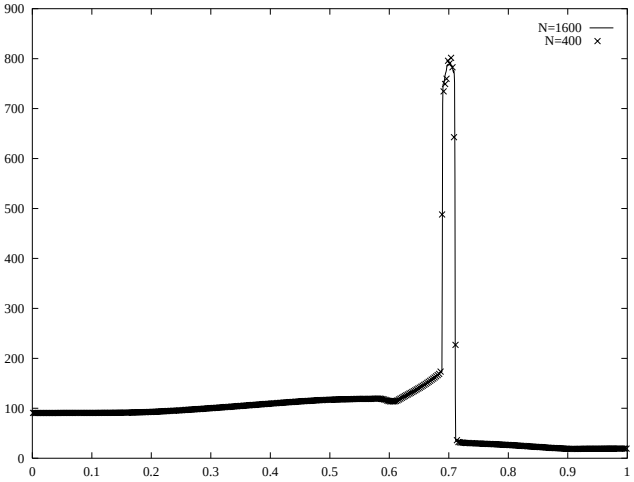

FIG. 4.6. *Problem* (4.2)–(4.3)*, pressure at* $T = 0.03$.

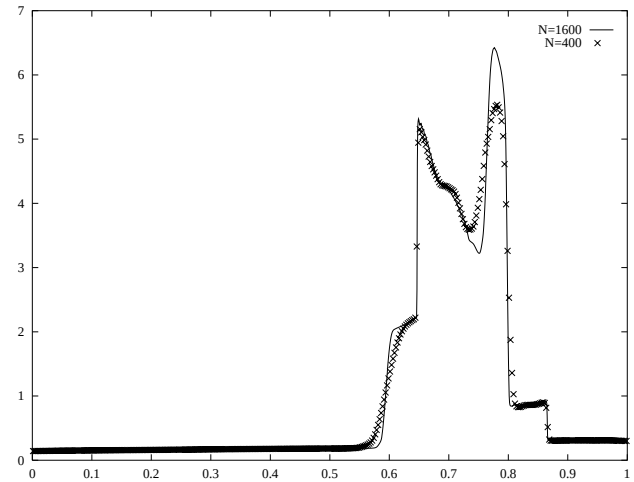

FIG. 4.7. *Problem* (4.2)–(4.3)*, density at* $T = 0.038$.

for an ideal gas, $\gamma = 1.4$, in the domain $[0, 2] \times [0, 0.5] \cup [0, 1] \times [0.5, 1]$, with the initial data corresponding to a vertical left-moving Mach 1.65 shock, positioned at $x = 1.375$. The initial shock propagates and then diffracts around a solid corner. Here ρ, u, v, p, and E are the density, the x- and y-velocities, the pressure, and the total energy, respectively.

We compute the solution at time $T = 0.5$, using the scheme (3.30)–(3.32), coupled with the reconstruction in [25]. The contour plots of the density for 128×64, 256×128, and 512×256 grid points are given in Figures 4.11, 4.12, and 4.13, respectively.

Note that as in [25], the results are obtained without using characteristic decomposition, dimensional splitting, or evolution of nonconservative quantities.

Example 5. 2-D Hamilton–Jacobi equation. We consider the initial value problem for the 2-D eikonal equation of geometric optics, which is a Hamilton–Jacobi

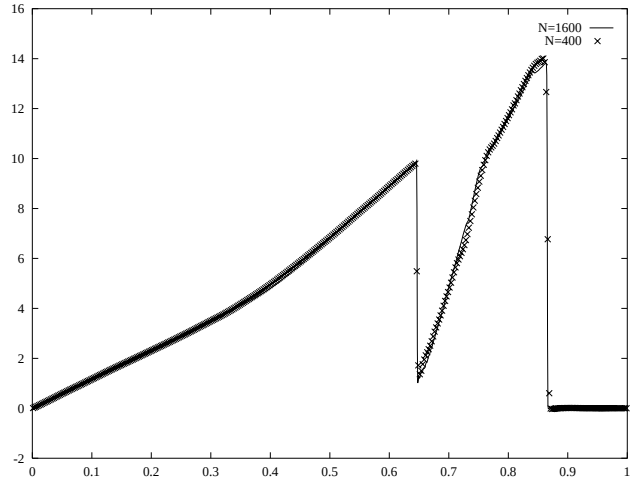

FIG. 4.8. *Problem* (4.2)–(4.3)*, velocity at* $T = 0.038$.

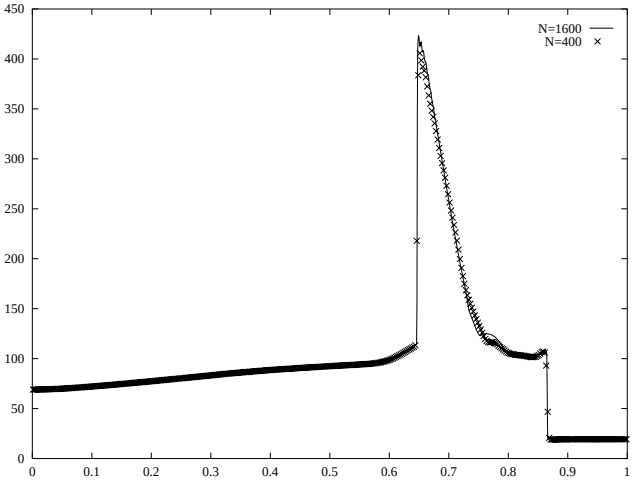

FIG. 4.9. *Problem* (4.2)–(4.3)*, pressure at* $T = 0.038$.

equation with a convex Hamiltonian,

$$\varphi_t+\sqrt{\varphi_x^2+\varphi_y^2+1}=0, \quad \varphi(x,y,0)=\frac{1}{4}(\cos(2\pi x)-1)(\cos(2\pi y)-1)-1, \ \ (x,y)\in[0,1]^2. \tag{4.6}$$

The numerical solution of (4.6) at time $T = 0.6$ (after formation of the singularity) has been computed by the 2-D second-order central-upwind scheme (3.49)–(3.50). The nonoscillatory nature of the computed solution and nearly perfect resolution of the singularity can be clearly seen in Figures 4.14–4.15.

4.3. 2-D incompressible Euler and Navier–Stokes equations. Here, we consider the incompressible Euler ($\nu = 0$) and Navier–Stokes ($\nu > 0$) equations

$$\vec{u}_t + (\vec{u}\cdot\nabla)\vec{u} + \nabla p = \nu\Delta\vec{u}, \tag{4.7}$$

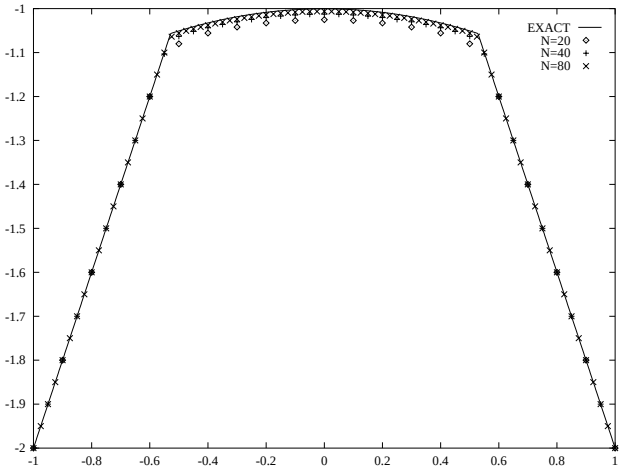

FIG. 4.10. *Problem* (4.4)*, solution at* $T = 1$.

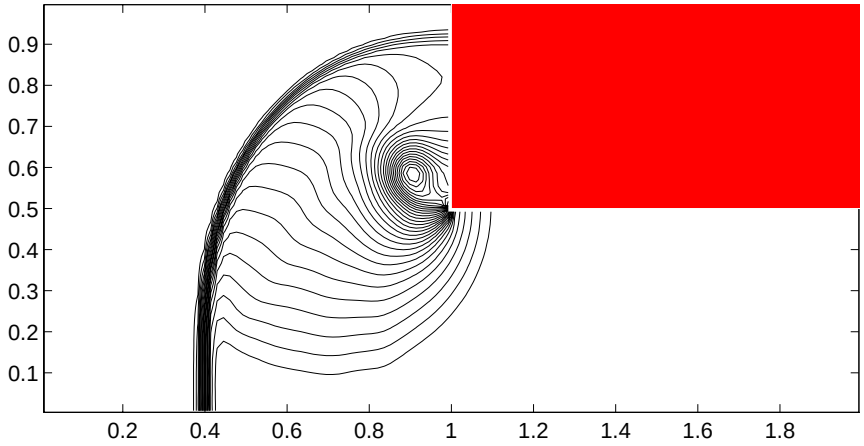

FIG. 4.11. *Equation* (4.5)*, density;* $T = 0.5$*,* 128×64 *grid,* 30 *contours.*

where p denotes the pressure and $\vec{u} = (u, v)$ is the divergence-free velocity field, satisfying $u_x + v_y = 0$. In the 2-D case, equation (4.7) admits an equivalent vorticity formulation, which can be written either in the conservative form,

$$\omega_t + (u\omega)_x + (v\omega)_y = \nu\Delta\omega, \tag{4.8}$$

or in the transport form,

$$\omega_t + u\omega_x + v\omega_y = \nu\Delta\omega, \tag{4.9}$$

where ω is the vorticity, $\omega := v_x - u_y$. Equation (4.8) can be viewed as a 2-D conservation law

$$\omega_t + f(\omega)_x + g(\omega)_y = \nu\Delta\omega, \tag{4.10}$$

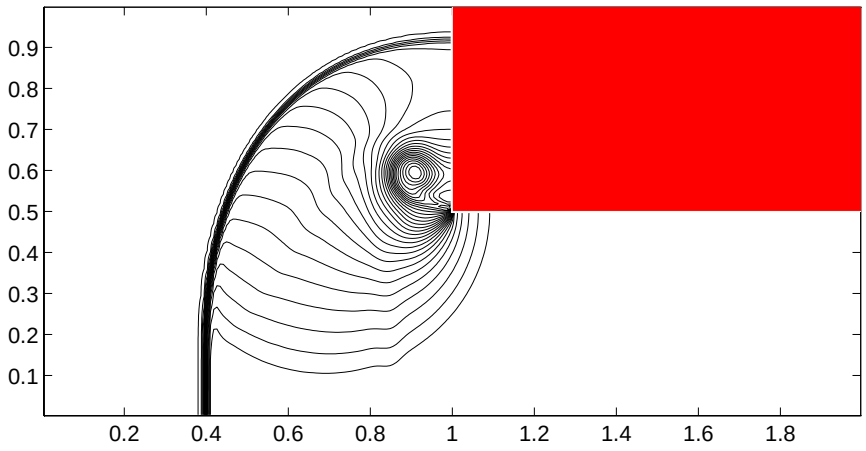

FIG. 4.12. *Equation* (4.5)*, density;* $T = 0.5$*,* 256×128 *grid,* 30 *contours.*

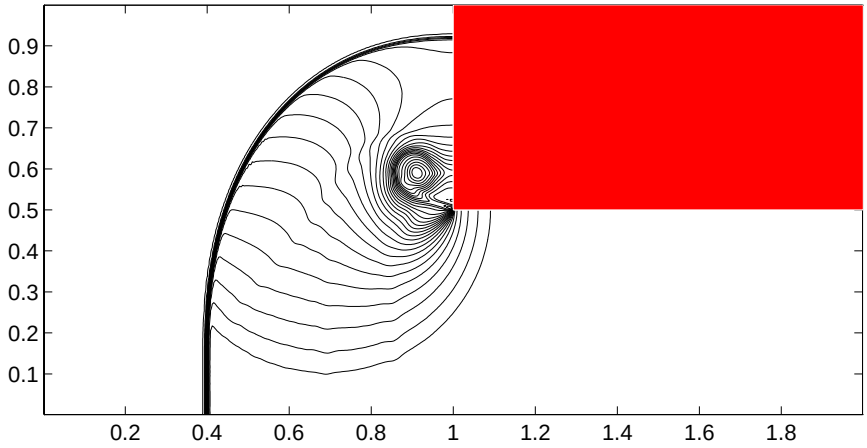

FIG. 4.13. *Equation* (4.5)*, density;* $T = 0.5$*,* 512×256 *grid,* 30 *contours.*

with a global flux $(f, g) := (u\omega, v\omega)$, while the transport equation (4.9) can be considered as a 2-D (viscous) Hamilton–Jacobi equation

$$\omega_t + H(\omega_x, \omega_y) = \nu\Delta\omega, \tag{4.11}$$

with a global Hamiltonian $H(\omega_x, \omega_y) = u\omega_x + v\omega_y$.

We propose two alternative Godunov-type semidiscrete central-upwind schemes for these two different formulations of the vorticity equation, (4.8) and (4.9). First, we consider (4.8) as a conservation law (4.10) and apply our 2-D third-order central-upwind scheme (3.30)–(3.32) to it. The resulting scheme has the conservative form

$$\frac{d}{dt}\bar{\omega}_{j,k}(t) = -\frac{H^x_{j+\frac{1}{2},k}(t) - H^x_{j-\frac{1}{2},k}(t)}{\Delta x} - \frac{H^y_{j,k+\frac{1}{2}}(t) - H^y_{j,k-\frac{1}{2}}(t)}{\Delta y} + \nu Q_{j,k}(t). \tag{4.12}$$

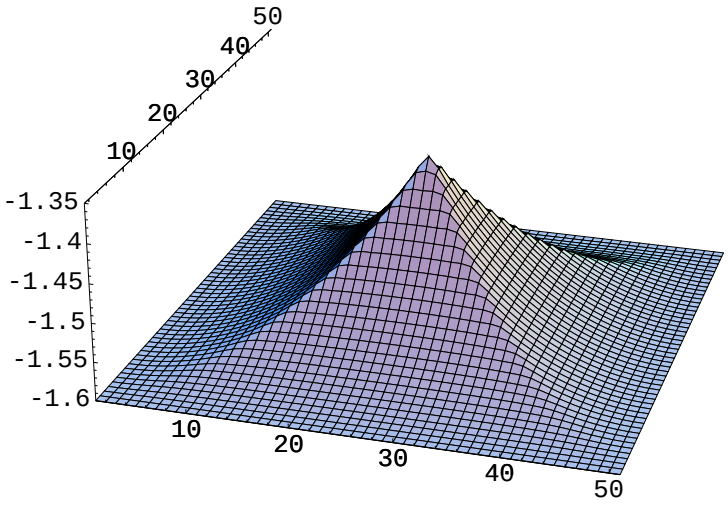

FIG. 4.14. *Problem* (4.6)*;* $T = 0.6$*,* 50×50 *grid.*

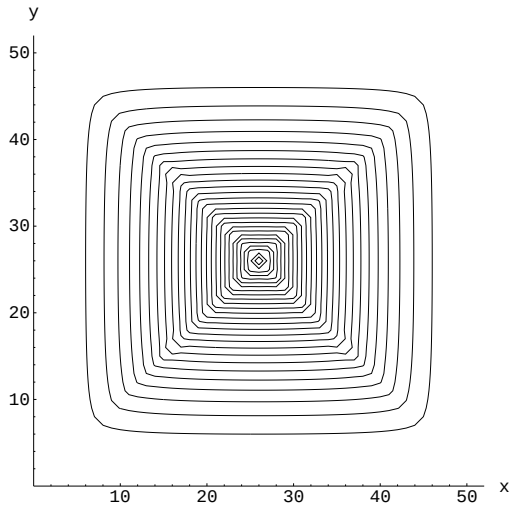

FIG. 4.15. *Contour plot.*

The following choice of the one-sided local speeds,

$$a^{\pm}_{j+\frac{1}{2},k} := (u_{j+\frac{1}{2},k})_{\pm}, \qquad b^{\pm}_{j,k+\frac{1}{2}} := (v_{j,k+\frac{1}{2}})_{\pm}, \tag{4.13}$$

yields the simplified numerical convection fluxes

$$H^x_{j+\frac{1}{2},k} := \frac{a^+_{j+\frac{1}{2},k}}{6\Big(a^+_{j+\frac{1}{2},k} - a^-_{j+\frac{1}{2},k}\Big)}\Big[u_{j+\frac{1}{2},k+\frac{1}{2}}\omega^{\mathrm{NE}}_{j,k} + 4u_{j+\frac{1}{2},k}\omega^{\mathrm{E}}_{j,k} + u_{j+\frac{1}{2},k-\frac{1}{2}}\omega^{\mathrm{SE}}_{j,k}\Big]$$

$$- \frac{a^-_{j+\frac{1}{2},k}}{6\Big(a^+_{j+\frac{1}{2},k} - a^-_{j+\frac{1}{2},k}\Big)}\Big[u_{j+\frac{1}{2},k+\frac{1}{2}}\omega^{\mathrm{NW}}_{j+1,k} + 4u_{j+\frac{1}{2},k}\omega^{\mathrm{W}}_{j+1,k} + u_{j+\frac{1}{2},k-\frac{1}{2}}\omega^{\mathrm{SW}}_{j+1,k}\Big], \tag{4.14}$$

and

$$H^y_{j,k+\frac12} := \frac{b^+_{j,k+\frac12}}{6\Big(b^+_{j,k+\frac12}-b^-_{j,k+\frac12}\Big)}\Big[v_{j-\frac12,k+\frac12}\omega^{\rm NW}_{j,k}+4v_{j,k+\frac12}\omega^{\rm N}_{j,k}+v_{j+\frac12,k+\frac12}\omega^{\rm NE}_{j,k}\Big]$$

$$-\frac{b^-_{j,k+\frac12}}{6\Big(b^+_{j,k+\frac12}-b^-_{j,k+\frac12}\Big)}\Big[v_{j-\frac12,k+\frac12}\omega^{\rm SW}_{j,k+1}+4v_{j,k+\frac12}\omega^{\rm S}_{j,k+1}+v_{j+\frac12,k+\frac12}\omega^{\rm SE}_{j,k+1}\Big]. \tag{4.15}$$

The diffusion term in (4.12) is obtained by the fourth-order central differencing,

$$\begin{aligned}Q_{j,k} &= \frac{-\bar\omega_{j+2,k}+16\bar\omega_{j+1,k}-30\bar\omega_{j,k}+16\bar\omega_{j-1,k}-\bar\omega_{j-2,k}}{12(\Delta x)^2}\\ &+\frac{-\bar\omega_{j,k+2}+16\bar\omega_{j,k+1}-30\bar\omega_{j,k}+16\bar\omega_{j,k-1}-\bar\omega_{j,k-2}}{12(\Delta y)^2}.\end{aligned} \tag{4.16}$$

The intermediate values of the velocities, required to compute the convection fluxes (4.14) and (4.15), are approximated by the fourth-order averaging, namely,

$$\begin{aligned}u_{j+\frac12,k} &= \frac{-u_{j+2,k}+9u_{j+1,k}+9u_{j,k}-u_{j-1,k}}{16},\\ v_{j,k+\frac12} &= \frac{-v_{j,k+2}+9v_{j,k+1}+9v_{j,k}-v_{j,k-1}}{16}.\end{aligned} \tag{4.17}$$

The velocities at the grid points, $\{u_{j,k},v_{j,k}\}$, are recovered from the computed vorticities $\{\omega_{j,k}\}$ at every time step. This is done with the help of the streamfunction ψ, such that $u=\psi_y$, $v=-\psi_x$, and $\Delta\psi=-\omega$. We solve this Poisson equation by the nine-point Laplacian approximation. Then, having the values of $\{\psi_{j,k}\}$, we compute the velocities

$$\begin{aligned}u_{j,k} &= \frac{-\psi_{j,k+2}+8\psi_{j,k+1}-8\psi_{j,k-1}+\psi_{j,k-2}}{12\Delta y},\\ v_{j,k} &= \frac{\psi_{j+2,k}-8\psi_{j+1,k}+8\psi_{j-1,k}-\psi_{j-2,k}}{12\Delta x}.\end{aligned} \tag{4.18}$$

This completes the construction of the "conservative" central-upwind scheme for the incompressible Euler and Navier–Stokes equations.

We now apply this scheme, coupled with the reconstruction in [25], to the Navier–Stokes equation (4.8) with $\nu=0.05$, augmented with the smooth periodic initial data

$$u(x,y,0)=-\cos x\sin y,\qquad v(x,y,0)=\sin x\cos y. \tag{4.19}$$

This test problem, proposed in [9], admits the exact classical solution, given by

$$u(x,y,t)=-e^{-2\nu t}\cos x\sin y,\qquad v(x,y,t)=e^{-2\nu t}\sin x\cos y.$$

In this numerical experiment, we check the accuracy of our scheme. The numerical solution is computed at time $T=2$, and the errors for the vorticity, measured in the L^∞-, L^1-, and L^2-norms, are presented in Table 4.2. These results indicate the expected third-order accuracy of the proposed scheme (4.12)–(4.18).

Next, we apply the scheme (4.12)–(4.18) together with the reconstruction in [25] to the Euler equation, (4.8) with $\nu=0$, subject to the $(2\pi,2\pi)$-periodic initial data

$$u(x,y,0)=\begin{cases}\tanh(\frac1\rho(y-\pi/2)), & y\le\pi,\\ \tanh(\frac1\rho(3\pi/2-y)), & y>\pi,\end{cases}\qquad v(x,y,0)=\delta\cdot\sin x. \tag{4.20}$$

TABLE 4.2

Accuracy test for the third-order "conservative" scheme for the Navier–Stokes equation (4.8), (4.19), $\nu = 0.05$*; errors at* $T = 2$.

$Nx \times Ny$	L^∞-error	rate	L^1-error	rate	L^2-error	rate
32×32	2.103e-03	–	2.761e-02	–	5.623e-03	–
64×64	2.788e-04	2.92	3.652e-03	2.92	7.404e-04	2.92
128×128	3.548e-05	2.97	4.636e-04	2.98	9.385e-05	2.98
256×256	4.444e-06	3.00	5.811e-05	3.00	1.176e-05	3.00

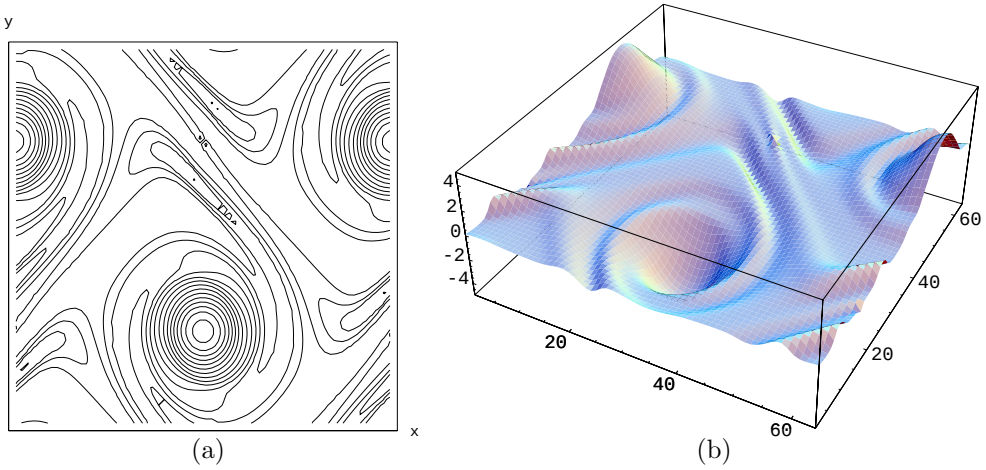

(a) (b)

FIG. 4.16. *Vorticity—"conservative" scheme,* 64×64.

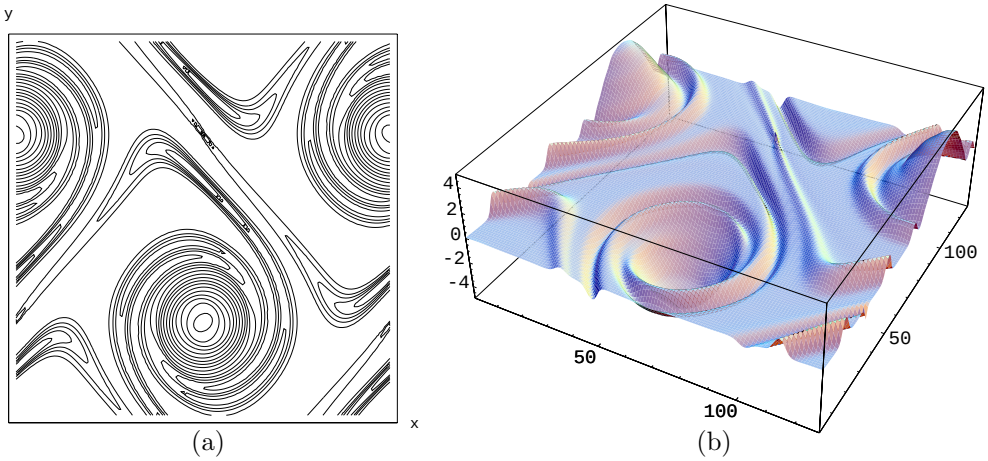

(a) (b)

FIG. 4.17. *Vorticity—"conservative" scheme,* 128×128.

This is the double shear-layer model problem, proposed in [7]. We take $\rho = \pi/15$ and $\delta = 0.05$. Figures 4.16(a) and 4.17(a) are the contour plots (30 contours) of the vorticity at time $T = 10$ with 64×64 and 128×128 grid points, respectively. The three-dimensional plots of the same results are shown in Figures 4.16(b) and 4.17(b). The performed numerical experiments demonstrate that our scheme provides a very high resolution. These results are comparable with the results obtained by the third-

TABLE 4.3
Accuracy test for the second-order "transport" scheme for the Navier–Stokes equation (4.9), (4.19), $\nu = 0.05$*; errors at* $T = 2$.

$Nx \times Ny$	L^∞-error	rate	L^1-error	rate	L^2-error	rate
32×32	5.559e-03	–	7.304e-02	–	1.492e-02	–
64×64	1.672e-03	1.73	2.265e-02	1.69	4.574e-03	1.71
128×128	4.531e-04	1.88	6.263e-03	1.85	1.250e-03	1.87
256×256	1.176e-04	1.95	1.644e-03	1.93	3.276e-04	1.93

order semidiscrete central scheme in [25].

The second alternative is to solve the vorticity equation in its transport form, (4.9), which can be viewed as a Hamilton–Jacobi equation (4.11).

We choose the one-sided local speeds to be

$$a^{\pm}_{j,k} := (u_{j,k})_{\pm}, \qquad b^{\pm}_{j,k} := (v_{j,k})_{\pm}, \tag{4.21}$$

and in this setting, our 2-D second-order central-upwind scheme (3.49)–(3.50) has the following simple form:

$$\begin{aligned}\frac{d}{dt}\omega_{j,k}(t) = &-\frac{a^-_{j,k}b^-_{j,k}(u_{j,k}\omega^+_x + v_{j,k}\omega^+_y) - a^-_{j,k}b^+_{j,k}(u_{j,k}\omega^+_x + v_{j,k}\omega^-_y)}{(a^+_{j,k} - a^-_{j,k})(b^+_{j,k} - b^-_{j,k})}\\ &+\frac{a^+_{j,k}b^-_{j,k}(u_{j,k}\omega^-_x + v_{j,k}\omega^+_y) - a^+_{j,k}b^+_{j,k}(u_{j,k}\omega^-_x + v_{j,k}\omega^-_y)}{(a^+_{j,k} - a^-_{j,k})(b^+_{j,k} - b^-_{j,k})} + \nu L_{j,k}.\end{aligned} \tag{4.22}$$

Here, $w^{\pm}_x$, $w^{\pm}_y$ are the right and the left derivatives in the x- and y-directions of the continuous piecewise polynomial reconstruction of $\{\omega_{j,k}\}$. The term $L_{j,k}$ stands for the standard central difference approximation of the linear viscous term, that is,

$$L_{j,k} = \frac{\omega_{j+1,k} - 2\omega_{j,k} + \omega_{j-1,k}}{(\Delta x)^2} + \frac{\omega_{j,k+1} - 2\omega_{j,k} + \omega_{j,k-1}}{(\Delta y)^2}. \tag{4.23}$$

As in the "conservative" scheme, we recover the velocities $\{u_{j,k}, v_{j,k}\}$ from the known values of the vorticity $\{\omega_{j,k}\}$, using the streamfunction approach. At each time step we solve the five-points Laplacian $\Delta\psi_{j,k} = -\omega_{j,k}$ and compute the velocities as follows:

$$u_{j,k} = \frac{\psi_{j,k+1} - \psi_{j,k-1}}{2\Delta y}, \qquad v_{j,k} = -\frac{\psi_{j+1,k} - \psi_{j-1,k}}{2\Delta x}. \tag{4.24}$$

We now apply this second-order "transport" scheme to the IBVP for the Navier–Stokes equation (4.9), (4.19) with $\nu = 0.05$. The numerical solution of this test problem is computed at time $T = 2$, and the L^∞-, L^1-, and L^2-errors for the vorticity are presented in Table 4.3. These results indicate the second-order convergence rate measured in all these norms. We would also like to point out that the absolute values of the errors here are about 10 times smaller than the corresponding errors obtained by the semidiscrete central scheme in [27, Table 6.1].

Finally, we test our scheme (4.21)–(4.24) on the double shear-layer problem (4.9), (4.20). The contour plots (30 contours) of the vorticity are shown in Figures 4.18(a), 4.19(a), and 4.20(a), where the computations are performed at time $T = 10$ with 64×64, 128×128, and 256×256 grid points. The corresponding three-dimensional plots are presented in Figures 4.18(b), 4.19(b), and 4.20(b).

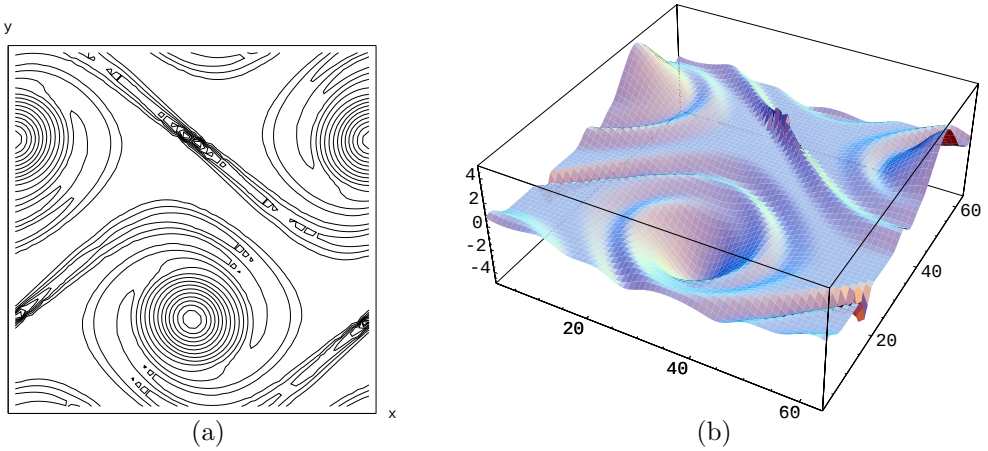

(a) (b)

FIG. 4.18. *Vorticity—"transport" scheme,* 64×64.

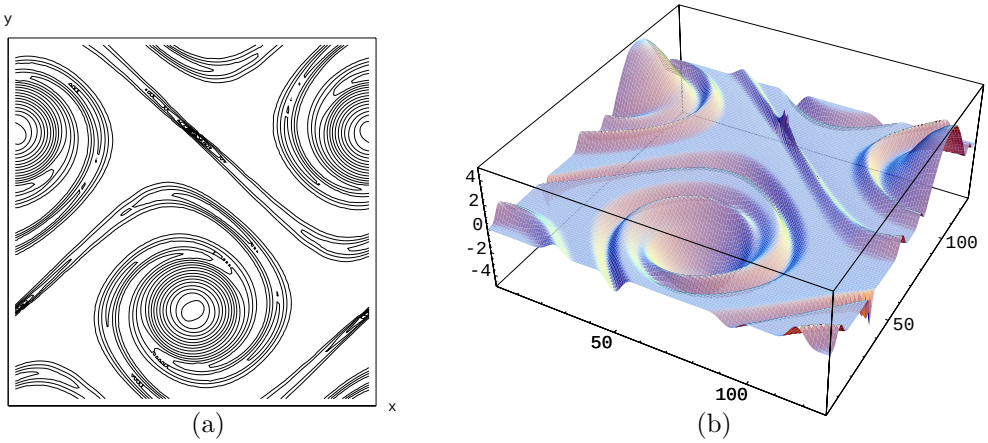

(a) (b)

FIG. 4.19. *Vorticity—"transport" scheme,* 128×128.

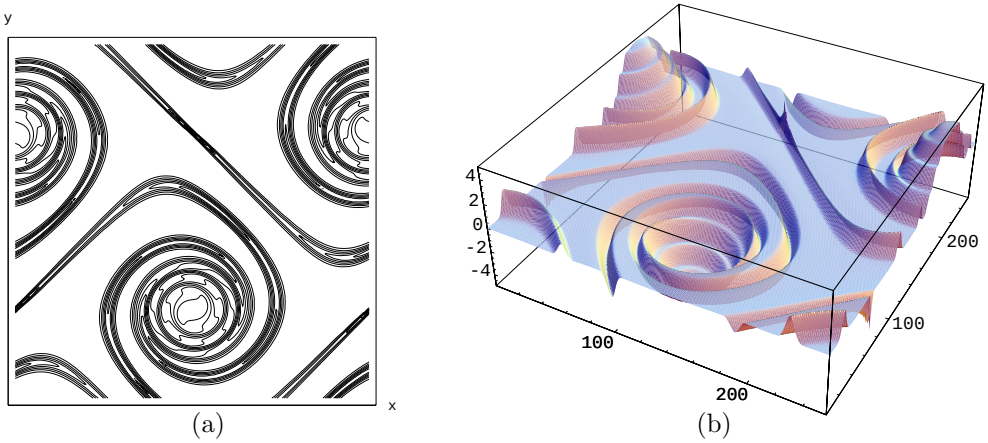

(a) (b)

FIG. 4.20. *Vorticity—"transport" scheme,* 256×256.

We would like to point out that our second-order "transport" scheme (4.21)–(4.24) has a very high resolution. The numerical experiments show that it is far superior to the second-order semidiscrete central scheme in [27, Figures 6.7–6.10]. This improvement is attributed to the smaller numerical viscosity present in the central-upwind scheme. Moreover, the resolution of (4.21)–(4.24) is almost as good as the resolution of our third-order "conservative" scheme (Figures 4.16 and 4.17).

As in [27, Figures 6.9–6.10], our numerical solution has spurious spikes, but of smaller heights. Also, the consequent mesh refinements (Figures 4.18–4.20) clearly demonstrate that the supports of these spikes diminish as the mesh size decreases.

Concluding remark. We have already mentioned the benefits of using the new central-upwind schemes in comparison to the central schemes in [26, 27, 24, 25]. Namely, they are *less dissipative*, and at the same time they retain the major advantages of central schemes—*simplicity* and *efficiency*.

In particular, the effect of the reduced numerical dissipation can be clearly seen when solving the incompressible Euler equation in its transport form. Moreover, in all of the numerical examples presented above, the achieved resolution is slightly better than the resolution obtained in [27, 24, 25].

The only drawback is the fact that the new schemes require the computation of both left and right local speeds, which increases the computational costs. However, the increase is not substantial, because as in any central scheme, our central-upwind schemes are Riemann-solver-free and do not require any computationally expensive characteristic decomposition.

REFERENCES

[1] R. Abgrall, *Numerical discretization of first-order Hamilton-Jacobi equation on triangular meshes*, Comm. Pure Appl. Math., 49 (1996), pp. 1339–1373.

[2] A.M. Anile, V. Romano, and G. Russo, *Extended hydrodynamical model of carrier transport in semiconductors*, SIAM J. Appl. Math., 61 (2000), pp. 74–101.

[3] P. Arminjon and M.-C. Viallon, *Généralisation du schéma de Nessyahu-Tadmor pour une équation hyperbolique à deux dimensions d'espace*, C. R. Acad. Sci. Paris Sér. I Math., 320 (1995), pp. 85–88.

[4] P. Arminjon, D. Stanescu, and M.-C. Viallon, *A two-dimensional finite volume extension of the Lax-Friedrichs and Nessyahu-Tadmor schemes for compressible flows*, in Proceedings of the 6th International Symposium on Computational Fluid Dynamics, Vol. 4, Lake Tahoe, CA, M. Hafez and K. Oshima, eds., 1995, pp. 7–14.

[5] P. Arminjon, M.-C. Viallon, and A. Madrane, *A finite volume extension of the Lax-Friedrichs and Nessyahu-Tadmor schemes for conservation laws on unstructured grids*, Int. J. Comput. Fluid Dyn., 9 (1997), pp. 1–22.

[6] P. Arminjon and M.-C. Viallon, *Convergence of a finite volume extension of the Nessyahu–Tadmor scheme on unstructured grids for a two-dimensional linear hyperbolic equation*, SIAM J. Numer. Anal., 36 (1999), pp. 738–771.

[7] J.B. Bell, P. Colella, and H.M. Glaz, *A second-order projection method for the incompressible Navier-Stokes equations*, J. Comput. Phys., 85 (1989), pp. 257–283.

[8] F. Bianco, G. Puppo, and G. Russo, *High-order central schemes for hyperbolic systems of conservation laws*, SIAM J. Sci. Comput., 21 (1999), pp. 294–322.

[9] A. Chorin, *Numerical solution of the Navier-Stokes equations*, Math. Comp., 22 (1968), pp. 745–762.

[10] L. Corrias, M. Falcone, and R. Natalini, *Numerical schemes for conservation laws via Hamilton-Jacobi equations*, Math. Comp., 64 (1995), pp. 555–580.

[11] M.G. Crandall and P.-L. Lions, *Two approximations of solutions of Hamilton-Jacobi equations*, Math. Comp., 43 (1984), pp. 1–19.

[12] B. Einfeldt, *On Godunov-type methods for gas dynamics,* SIAM J. Numer. Anal., 25 (1988), pp. 294–318.

[13] B. Engquist and O. Runborg, *Multi-phase computations in geometrical optics*, J. Comput. Appl. Math., 74 (1996), pp. 175–192.
[14] K.O. Friedrichs, *Symmetric hyperbolic linear differential equations*, Comm. Pure Appl. Math., 7 (1954), pp. 345–392.
[15] A. Harten, *High resolution schemes for hyperbolic conservation laws*, J. Comput. Phys., 49 (1983), pp. 357–393.
[16] A. Harten, B. Engquist, S. Osher, and S.R. Chakravarthy, *Uniformly high order accurate essentially non-oscillatory schemes* III, J. Comput. Phys., 71 (1987), pp. 231–303.
[17] A. Harten, P.D. Lax, and B. van Leer, *On upstream differencing and Godunov-type schemes for hyperbolic conservation laws*, SIAM Rev., 25 (1983), pp. 35–61.
[18] G.-S. Jiang and C.-W. Shu, *Efficient implementation of weighted ENO schemes*, J. Comput. Phys., 126 (1996), pp. 202–228.
[19] G.-S. Jiang and E. Tadmor, *Nonoscillatory central schemes for multidimensional hyperbolic conservation laws*, SIAM J. Sci. Comput., 19 (1998), pp. 1892–1917.
[20] R. Kupferman, *Simulation of viscoelastic fluids: Couette-Taylor flow*, J. Comput. Phys., 147 (1998), pp. 22–59.
[21] R. Kupferman, *A numerical study of the axisymmetric Couette–Taylor problem using a fast high-resolution second-order central scheme*, SIAM J. Sci. Comput., 20 (1998), pp. 858–877.
[22] R. Kupferman and E. Tadmor, *A fast high-resolution second-order central scheme for incompressible flows*, Proc. Natl. Acad. Sci. USA, 94 (1997), pp. 4848–4852.
[23] A. Kurganov, *Conservation Laws: Stability of Numerical Approximations and Nonlinear Regularization*, Ph.D. Thesis, Tel-Aviv University, Israel, 1997.
[24] A. Kurganov and D. Levy, *A third-order semidiscrete central scheme for conservation laws and convection-diffusion equations*, SIAM J. Sci. Comput., 22 (2000), pp. 1461–1488.
[25] A. Kurganov and G. Petrova, *A third-order semi-discrete genuinely multidimensional central scheme for hyperbolic conservation laws and related problems*, Numer. Math., to appear.
[26] A. Kurganov and E. Tadmor, *New high-resolution central schemes for nonlinear conservation laws and convection-diffusion equations*, J. Comput. Phys., 160 (2000), pp. 241–282.
[27] A. Kurganov and E. Tadmor, *New high-resolution semi-discrete central schemes for Hamilton-Jacobi equations*, J. Comput. Phys., 160 (2000), pp. 720–742.
[28] P.D. Lax, *Weak solutions of nonlinear hyperbolic equations and their numerical computation*, Comm. Pure Appl. Math., 7 (1954), pp. 159–193.
[29] B. van Leer, *Towards the ultimate conservative difference scheme,* V. *A second order sequel to Godunov's method*, J. Comput. Phys., 32 (1979), pp. 101–136.
[30] D. Levy, G. Puppo, and G. Russo, *Central WENO schemes for hyperbolic systems of conservation laws,* M2AN Math. Model. Numer. Anal., 33 (1999), pp. 547–571.
[31] D. Levy, G. Puppo, and G. Russo, *A third order central WENO scheme for* 2D *conservation laws*, Appl. Numer. Math., 33 (2000), pp. 407–414.
[32] D. Levy, G. Puppo, and G. Russo, *Compact central WENO schemes for multidimensional conservation laws*, SIAM J. Sci. Comput., 22 (2000), pp. 656–672.
[33] D. Levy and E. Tadmor, *Non-oscillatory central schemes for the incompressible* 2-D *Euler equations*, Math. Res. Lett., 4 (1997), pp. 1–20.
[34] K.-A. Lie and S. Noelle, *Remarks on High-Resolution Non-Oscillatory Central Schemes for Multi-Dimensional Systems of Conservation Laws. Part* I: *An Improved Quadrature Rule for the Flux-Computation*, SFB256 preprint 679, Bonn University, Germany.
[35] C.-T. Lin and E. Tadmor, *L^1-stability and error estimates for approximate Hamilton-Jacobi solutions*, Numer. Math., 87 (2001), pp. 701–735.
[36] C.-T. Lin and E. Tadmor, *High-resolution nonoscillatory central schemes for Hamilton–Jacobi equations*, SIAM J. Sci. Comput., 21 (2000), pp. 2163–2186.
[37] X.-D. Liu and S. Osher, *Nonoscillatory high order accurate self-similar maximum principle satisfying shock capturing schemes.* I, SIAM J. Numer. Anal., 33 (1996), pp. 760–779.
[38] X.-D. Liu, S. Osher, and T. Chan, *Weighted essentially non-oscillatory schemes*, J. Comput. Phys., 115 (1994), pp. 200–212.
[39] X.-D. Liu and E. Tadmor, *Third order nonoscillatory central scheme for hyperbolic conservation laws*, Numer. Math., 79 (1998), pp. 397–425.
[40] H. Nessyahu and E. Tadmor, *Non-oscillatory central differencing for hyperbolic conservation laws*, J. Comput. Phys., 87 (1990), pp. 408–463.
[41] S. Noelle, *A comparison of third and second order accurate finite volume schemes for the two-dimensional compressible Euler equations*, in Proceedings of the Seventh International Conference on Hyperbolic Problems, Zürich, 1998, Internat. Ser. Numer. Math.

129, Birkhäuser, Basel, pp. 757–766.
[42] S. Osher and C.-W. Shu, *High-order essentially nonoscillatory schemes for Hamilton-Jacobi equations*, SIAM J. Numer. Anal., 28 (1991), pp. 907–922.
[43] S. Osher and E. Tadmor, *On the convergence of difference approximations to scalar conservation laws*, Math. Comp., 50 (1988), pp. 19–51.
[44] V. Romano and G. Russo, *Numerical solution for hydrodynamical models of semiconductors*, Math. Models Methods Appl. Sci., 10 (2000), pp. 1099–1120.
[45] C.-W. Shu, *Total-variation-diminishing time discretizations*, SIAM J. Sci. Statist. Comput., 9 (1988), pp. 1073–1084.
[46] C.-W. Shu, *Numerical experiments on the accuracy of ENO and modified ENO schemes*, J. Sci. Comput., 5 (1990), pp. 127–149.
[47] C.-W. Shu and S. Osher, *Efficient implementation of essentially non-oscillatory shock-capturing schemes*, J. Comput. Phys., 77 (1988), pp. 439–471.
[48] P.E. Souganidis, *Approximation schemes for viscosity solutions of Hamilton-Jacobi equations*, J. Differential Equations., 59 (1985), pp. 1–43.
[49] Y.C. Tai, S. Noelle, N. Gray, and K. Hutter, *Shock Capturing and Front Tracking Methods for Granular Avalanches*, SFB256 Preprint 678, Bonn University, Germany; J. Comput. Phys., to appear.
[50] B. Wendroff, *Approximate Riemann solvers, Godunov schemes, and contact discontinuities*, in *Godunov Methods: Theory and Applications*, E. F. Toro, ed., Kluwer Academic/Plenum Publishers, New York, to appear.
[51] P. Woodward and P. Colella, *The numerical solution of two-dimensional fluid flow with strong shocks*, J. Comput. Phys., 54 (1988), pp. 115–173.